ANTIOXIDANTS & REDOX SIGNALING
Volume 39, Numbers 7–9, 2023

DOI: 10.1089/ars.2022.0105

ORIGINAL RESEARCH COMMUNICATION

AUF1 Recognizes 8-Oxo-Guanosine Embedded in DNA and Stimulates APE1 Endoribonuclease Activity

Matilde Clarissa Malfatti,[1] Marta Codrich,[1] Emiliano Dalla,[1] Chiara D'Ambrosio,[2] Francesca Storici,[3] Andrea Scaloni,[2] and Gianluca Tell[1]

Abstract

Aims: The existence of modified ribonucleotide monophosphates embedded in genomic DNA, as a consequence of oxidative stress conditions, including 8-oxo-guanosine and ribose monophosphate abasic site (rAP), has been recently highlighted by several works and associated with oxidative stress conditions. Although human apurinic-apyrimidinic endodeoxyribonuclease 1 (APE1), a key enzyme of the base-excision repair pathway, repairs rAP sites and canonical deoxyribose monophosphate abasic sites with similar efficiency, its incision-repairing activity on 8-oxo-guanosine is very weak. The aims of this work were to: (i) identify proteins able to specifically bind 8-oxo-guanosine embedded in DNA and promote APE1 endoribonuclease activity on this lesion, and (ii) characterize the molecular and biological relevance of this interaction using human cancer cell lines.
Results: By using an unbiased proteomic approach, we discovered that the AU-rich element RNA-binding protein 1 (AUF1) actively recognizes 8-oxo-guanosine and stimulates the APE1 enzymatic activity on this DNA lesion. By using orthogonal approaches, we found that: (i) the interaction between AUF1 and APE1 is modulated by H_2O_2-treatment; (ii) depletion of APE1 and AUF1 causes the accumulation of single- and double-strand breaks; and (iii) both proteins are involved in modulating the formation of DNA:RNA hybrids.
Innovation: These results establish unexpected functions of AUF1 in modulating genome stability and improve our knowledge of APE1 biology with respect to 8-oxo-guanosine embedded in DNA.
Conclusion: By showing a novel function of AUF1, our findings shed new light on the process of genome stability in mammalian cells toward oxidative stress-related damages. *Antioxid. Redox Signal.* 39, 411–431.

Keywords: DNA/RNA damage and repair, protein–protein interaction, APE1, AUF1, 8-oxo-guanosine, R-loop, DNA:RNA hybrids

Introduction

A RECURRENT DNA damage is represented by the presence of ribonucleosides monophosphate (rNMPs) incorporated within DNA (Jinks-Robertson and Klein, 2015), a frequent phenomenon that counts 1 rNMP every 700 deoxyribonucleosides monophosphate (dNMPs) (Sparks et al., 2012). One leading cause of this incorporation principally involves the replication process, during which DNA polymerases can incorporate ribonucleosides triphosphate (rNTPs) in place of deoxyribonucleosides triphosphate (dNTPs) into the nascent strand, in a cellular context in which the stoichiometry of the process is in favor of rNTPs (Brown and Suo, 2011; McElhinny et al., 2010; Nick McElhinny et al., 2010; Williams et al., 2012).

Another source of rNMPs incorporation is the partial removal of RNA primers, needed for priming the replication process of the lagging strand (Clausen et al., 2015). Finally,

[1]Laboratory of Molecular Biology and DNA Repair, Department of Medicine (DAME), University of Udine, Udine, Italy.
[2]Proteomics, Metabolomics and Mass Spectrometry Laboratory, Institute for the Animal Production System in the Mediterranean Environment (ISPAAM), National Research Council (CNR) of Italy, Portici, Italy.
[3]School of Biological Sciences, Georgia Institute of Technology, Atlanta, Georgia, USA.

Innovation

The data included in this work establish novel important functions of AU-rich element RNA-binding protein 1 (AUF1) in modulating genome stability and improve our knowledge of apurinic-apyrimidinic endodeoxyribonuclease 1 (APE1) biology. Specifically, our data suggest a role of AUF1 as a stabilizer of 8-oxo-guanosine embedded in DNA, stimulating the endoribonuclease activity by APE1 (Fig. 1). Interestingly, we discovered that: (i) AUF1 is a novel interactor of APE1; (ii) the AUF1–APE1 interaction is modulated on and protects from oxidative stress induced damage; and (iii) the depletion of AUF1 and APE1 is associated with an accumulation of abasic sites, formation of double-strand breaks, and generation of DNA:RNA hybrids.

although not well characterized yet, a conversion from deoxyribose to ribose can occur in the cellular pool of nucleotides or directly into the DNA, this being critical for the presence of rNMPs embedded in DNA (Randerath et al., 1992).

Although the presence of rNMPs in the genome has been proposed to facilitate the mismatch repair pathway and promote the mating-type switch in fission yeast (Potenski and Klein, 2014), their occurrence is mainly considered harmful for several cellular functions, with detrimental effects on cell survival. rNMPs have been confirmed to have a destabilizing conformational effect on their site of incorporation, due to the additional presence of the 2′-OH group on the ribose sugar (Chiu et al., 2014; Koh et al., 2015b; Meroni et al., 2017).

The consequent alteration of the DNA backbone causes a blockage of transcription and replication, as well as of nucleosome assembly, which are all events necessary for cell survival (Agarwal and Miller, 2016). Moreover, the accumulation of rNMPs likely induces the triggering of the DNA damage signaling, through spontaneous hydrolysis of the free 2′-OH, which could lead to the formation of single-strand breaks (Kellner and Luke, 2020).

For all these reasons, a specific repair pathway, called ribonucleotide excision repair (RER), is responsible for the recognition and repair of rNMPs (Kellner and Luke, 2020). On RER-deficiency, topoisomerase 1 (Top1) has been demonstrated to act as a backup in rNMP removal (Cerritelli et al., 2020; Cho and Jinks-Robertson, 2018; Li et al., 2019; Williams and Kunkel, 2018). In this context, several studies have demonstrated that other repair pathways, including nucleotide excision repair, mismatch repair, and base excision repair (BER), do not possess any functional role in the canonical rNMPs recognition and excision (Cai et al., 2014; Cilli et al., 2015; Malfatti et al., 2017; Vaisman et al., 2013).

Recently, increased attention has been paid to non-canonical modified rNMPs embedded in DNA and, mostly, to their repair mechanisms (Cilli et al., 2015; Ghodke et al., 2020; Malfatti et al., 2017). Although not fully investigated, modified rNMPs, including ribose monophosphate abasic sites (rAP, either apurinic or apyrimidinic) and oxidized rNMPs (r-8oxo-G), can be generated, as in the case of dNMPs. The genome of human cells suffers about 1000–100,000 oxidative lesions per day, and one of the most common defects in this category is represented by 7,8-dihydro-8-oxoguanine (Jackson and Bartek, 2009).

Moreover, deoxyribose monophosphate abasic sites are the most frequent lesions in human cells, with estimates of ~10,000–20,000 per day (Nakamura et al., 1998). Recently, Smith et al. (2020) have demonstrated that r-8oxo-GTP is inserted at a rate similar to those of other common replication errors (*i.e.,* ribonucleotide and mismatch insertions), with similar retention of conformation and base pairing of d-8oxo-GTP, thus highlighting its potential mutagenicity. This occurs even though polymerase β (Pol β) has a diminished catalytic efficiency for r-8oxo-GTP, compared to canonical dNTPs, due to an impaired Pol β closure (Batra et al., 2016).

The interest for these non-canonical rNMPs is largely emerging, as recently demonstrated by a work investigating the impact of a damaged analog of rATP, namely 1, N^6-ethenoadenosine (1, N^6-εrA), on translesion synthesis (Ghodke et al., 2020). RNA abasic sites in yeast and human cells are not rare as previously assumed, counting about 3 rAP sites per 1,000,000 ribonucleotides (Liu et al., 2020).

Surprisingly, we found that RNase H2 is unable to repair either rAP or 8-oxo-guanosine sites embedded in DNA (Malfatti et al., 2019; Malfatti et al., 2017), whereas apurinic-apyrimidinic endodeoxyribonuclease 1 (APE1), the main AP-endonuclease enzyme belonging to the BER pathway, efficiently processes rAP sites and, despite showing a weak saline-dependent endo- and exo-nuclease activity, also 8-oxo-guanosine sites through its nucleotide incision repair (NIR) activity (Malfatti et al., 2017).

Recent publications have demonstrated a strong relevance of non-canonical rNMPs in the DNA repair field, but a lack of information exists regarding their mechanisms of recognition and the corresponding enzymatic processing. In the case of 8-oxo-guanosine, additional recognition and processing mechanisms should be active and might cooperate with APE1 to guarantee an efficient repair process and to increase the efficiency of its enzymatic activity.

Here, we have demonstrated that AU-rich element RNA-binding protein 1 (AUF1) can efficiently bind 8-oxo-guanosine, stabilizing the region containing it, and promoting the APE1 enzymatic activity on it. Moreover, we have found that AUF1 is an interactor of APE1, as demonstrated by *in vitro* and *in vivo* analyses. Interestingly, this interaction is modulated by H_2O_2 and $KBrO_3$ treatments and plays a biological role during cell response to oxidative stress and in the formation of DNA:RNA (D:R) hybrids. By showing a novel function of AUF1, these findings shed new light on the process of accumulation and repair of 8-oxo-guanosine embedded in DNA in mammalian cells (Fig. 1).

Results

Proteomics reveal AUF1 as one of several proteins recognizing 8-oxo-guanosine sites embedded in DNA

The first aim of this study was to provide details on the molecular mechanism used for repairing 8-oxo-guanosine site embedded in DNA, and to identify specific regulatory proteins deputed to process this highly mutagenic lesion or to promote the NIR activity of APE1 on this substrate.

First, we exploited a Southwestern blot (SWB) analysis to compare the ability of nuclear proteins from HEK293T cells to differentially recognize oligonucleotide substrates containing 8-oxo-guanosine (ds_r8oxoG:dC oligonucleotide) in comparison to rAP (ds_rF:dC) or guanosine (ds_rG:dC) embedded in DNA. The proteins blotted on the membrane

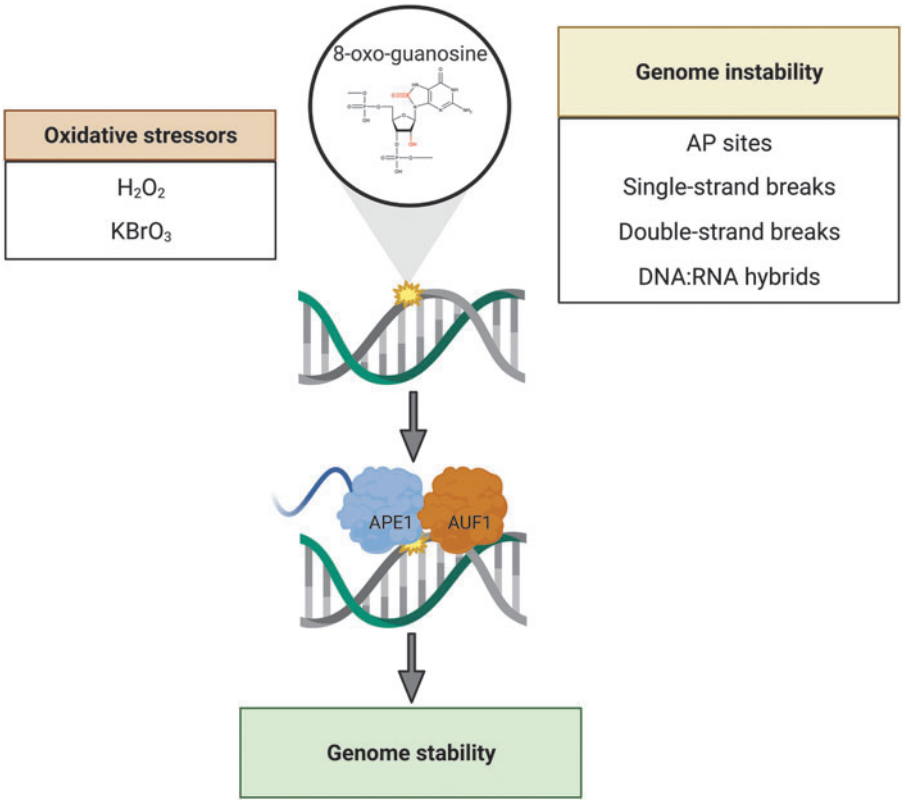

FIG. 1. APE1 and AUF1 cooperate for the repair of 8-oxo-guanosine embedded in DNA and for restoring genome stability. A summary graphic model illustrates an unrepaired 8-oxo-guanosine incorporated in DNA, possibly generated by exposure to oxidative stressors, such as H_2O_2 and $KBrO_3$, which cause genome instability with an accumulation of AP sites, single- and double-strand breaks, and DNA:RNA hybrids. On processing by the APE1 and AUF1, the DNA damage is restored. AP, apurinic and apyrimidinic site; APE1, apurinic-apyrimidinic endodeoxyribonuclease 1; AUF1, AU-rich element RNA-binding protein 1. Created with BioRender.com

were renatured by serial dilutions of guanidine hydrochloride (Gdn-HCl) up to reach their native condition, and then incubated with the fluorescent oligonucleotides (Fig. 2A). SWB data are shown in Supplementary Figure S1A.

Each band corresponded to the fluorescence of each oligonucleotide used, bound to one or more proteins having the same molecular mass. As expected, a high number of bands was detectable in the three lanes, corresponding to several different proteins able to bind DNA or the specific modification on DNA. The high number of detected bands, reflecting the high complexity of species bound to the 8-oxo-guanosine, prompted us to adopt a different experimental approach based on protein isolation through affinity chromatography and molecular identification with mass spectrometry-based proteomics.

FIG. 2. AUF1 binds to 8-oxo-guanosine sites embedded in DNA and stimulates the binding of APE1 to the ds_r8oxoG:dC substrate promoting its processing. (A) Representation of 25-mer ODNs in which a modified base is embedded at the 13th position. Specifically, a ribo-G (ds_rG:dC), a ribo-monophosphate abasic site (ds_rF:dC), an 8-oxoguanosine (ds_r8oxoG:dC), and a deoxy-G (ds_dG:dC). Ribonucleotides are represented in *red*, whereas deoxyribonucleotides are depicted in *blue*. F corresponds to tetrahydrofuran mimicking the abasic site, whereas 8oxo to oxidized G. IRDye corresponds to the phosporamidite-labelling moiety able to emit fluorescence at 700 or 800 nm. 5′- and 3′-ends are indicated. The biotin molecule is indicated with a cartoon labeled as Biotin at the 5′-side of the complementary strand. Below each ODN scheme, the name is indicated. **(B)** Starting from HEK293T NCE, a biotin/streptavidin-based approach was used to capture proteins binding to specific DNA modifications through a dedicated immunotrapping procedure with magnetic beads coupled to nanoLC-ESI-Q-Orbitrap-MS/MS-based proteomic analysis. Created with BioRender.com **(C)** Immunoblotting analysis of the protein fractions eluted 300 and 400 m*M* NaCl from the following probes: ds_rG:dC_Biot, ds_rF:dC_Biot and ds_r8oxoG:dC_Biot with anti-AUF1 (IB: AUF1). NCE were used as AUF1 signal control. On the *left* side of the *panel*, the molecular marker (M) is shown, whose mass value is expressed in kDa. Below the *panel*, each lane is sequentially numbered. **(D)** Cross-linking analysis of different amounts of recombinant AUF1 protein on the ds_r8oxoG:dC and ds_dG:dC substrates (25 n*M*). The band corresponding to the DNA-cross-linked proteins is indicated with an *arrow*. **(E)** EMSA of different amounts of recombinant AUF1 protein on the ds_dG:dC and ds_r8oxoG:dC substrates (25 n*M*). The *arrow* indicates the shift of the oligonucleotide in the presence of AUF1. **(F)** *Left*, EMSA of different amounts of the recombinant AUF1 and APE1 proteins on the ds_r8oxoG:dC substrate (25 n*M*). A single *asterisk* indicates the shift of the oligonucleotide when bound by AUF1, whereas two and three *asterisks* indicate different shifts of oligonucleotides in the presence of APE1. *Right*, a histogram reports the average of the differential signals of the APE1- and AUF1-binding on ds_r8oxoG:dC, expressed as arbitrary units. **(G)** Endonuclease activity analysis of the recombinant APE1WT and its mutants (25 n*M*), including NΔ33 and E96A, and the AUF1 (250 n*M*) with the ds_r8oxoG:dC substrate (25 n*M*). S and P indicate substrate and products, respectively. The *arrow* points out to wells of gel in which a signal is detected. **(H)** Endonuclease activity analysis of the recombinant APE1 protein (25 n*M*) and different amounts of the recombinant AUF1 protein on the ds_r8oxoG:dC substrate (25 n*M*) as measured after digesting the reaction mixture with 1 μg of proteinase K. S and P indicate substrate and products. The *arrow* points out to wells of gel in which a signal was detected in **(G)**. EMSA, electrophoretic mobility shift analysis; MS/MS, tandem mass spectrometry; NCE, nuclear cell extracts; ODN, oligonucleotide; WT, wild type.

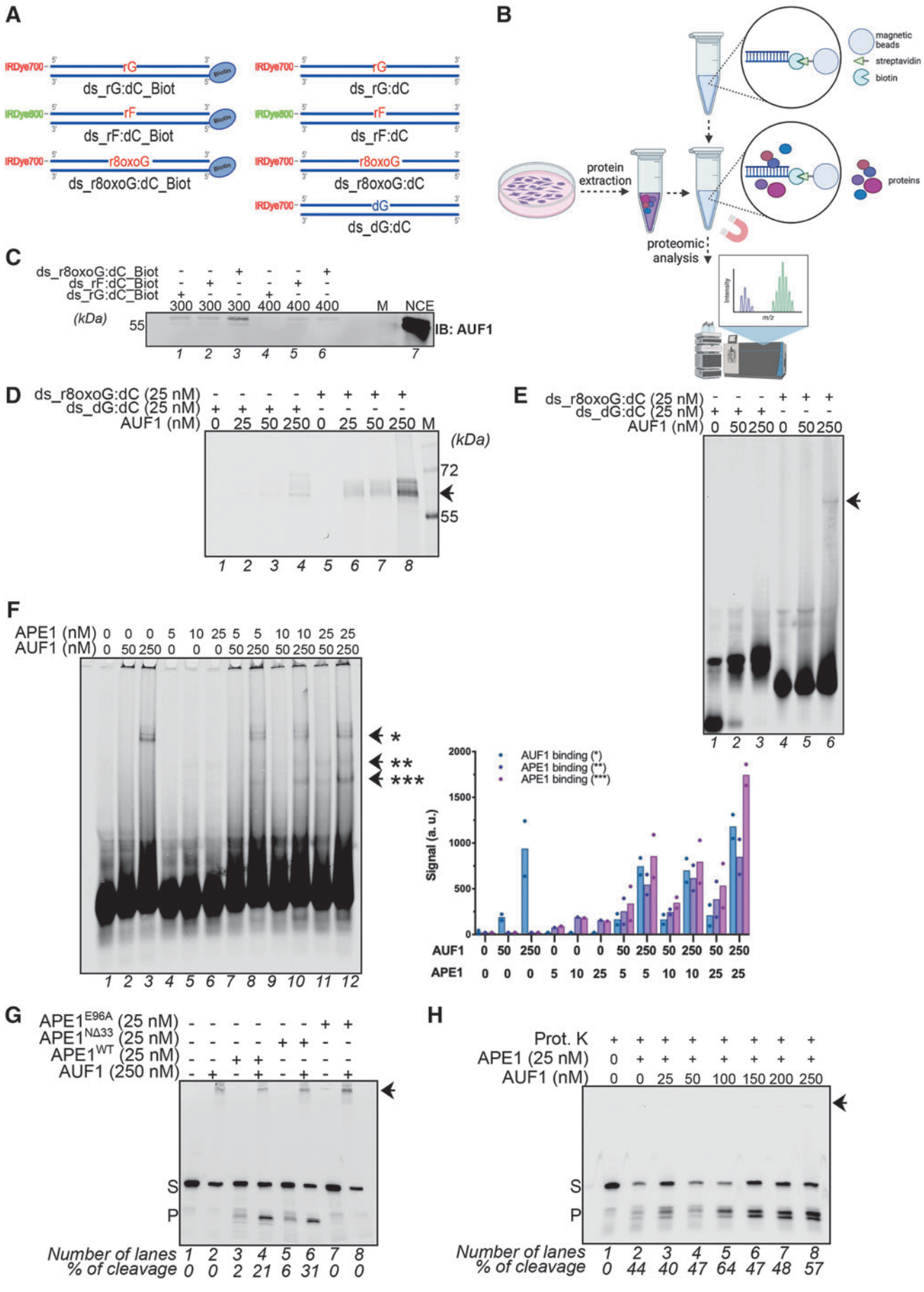
A
IRDye700
IRDye800
rG
rF
r8oxoG
dG
Biotin
ds_rG:dC_Biot
ds_rF:dC_Biot
ds_r8oxoG:dC_Biot
ds_rG:dC
ds_rF:dC
ds_r8oxoG:dC
ds_dG:dC
B
magnetic beads
streptavidin
biotin
protein extraction
proteins
proteomic analysis
C
ds_r8oxoG:dC_Biot
ds_rF:dC_Biot
ds_rG:dC_Biot
300 300 300 400 400 400 M NCE
(kDa)
55
IB: AUF1
1 2 3 4 5 6 7
D
ds_r8oxoG:dC (25 nM)
ds_dG:dC (25 nM)
AUF1 (nM) 0 25 50 250 0 25 50 250 M
(kDa)
72
55
1 2 3 4 5 6 7 8
E
ds_r8oxoG:dC (25 nM)
ds_dG:dC (25 nM)
AUF1 (nM) 0 50 250 0 50 250
1 2 3 4 5 6
F
APE1 (nM) 0 0 0 5 10 25 5 5 10 10 25 25
AUF1 (nM) 0 50 250 0 0 0 50 250 50 250 50 250
*
**
***
1 2 3 4 5 6 7 8 9 10 11 12
AUF1 binding (*)
APE1 binding (**)
APE1 binding (***)
Signal (a. u.)
2000
1500
1000
500
0
AUF1 0 50 250 0 0 0 50 250 50 250 50 250
APE1 0 0 0 5 10 25 5 5 10 10 25 25
G
APE1E96A (25 nM)
APE1NΔ33 (25 nM)
APE1WT (25 nM)
AUF1 (250 nM)
S
P
Number of lanes 1 2 3 4 5 6 7 8
% of cleavage 0 0 2 21 6 31 0 0
H
Prot. K
APE1 (25 nM)
AUF1 (nM) 0 0 25 50 100 150 200 250
S
P
Number of lanes 1 2 3 4 5 6 7 8
% of cleavage 0 44 40 47 64 47 48 57

For this reason, we used a biotin-streptavidin affinity chromatography strategy schematically illustrated in Figure 2B. Briefly, we used the same oligonucleotides (ds_r8oxoG:dC, ds_rF:dC, and ds_rG:dC) as cited earlier but bearing a biotin molecule at the 5′-end of the non-modified complementary oligonucleotide (Fig. 2A). Then, each double-stranded oligonucleotide was incubated with nuclear cell extracts (NCE) from HEK293T cells to allow the binding between the oligonucleotide and the proteins. The resulting DNA-protein complexes were subsequently isolated by incubation with specific streptavidin-coated magnetic Dynabeads™. The elution was achieved by increasing concentrations of NaCl, ranging from 75 m*M* to 1 *M*. The experiment was performed in parallel for the three oligonucleotides described earlier.

Fractions from streptavidin-coated magnetic Dynabeads loaded in parallel with ds_r8oxoG:dC_Biot, ds_rF:dC_Biot and ds_rG:dC_Biot incubated with NCE from HEK293T cells, and finally eluted with 300 and 400 m*M* NaCl were further analyzed for protein content by nanoLC-ESI-Q-Orbitrap-MS/MS. On the whole, the proteomic analysis identified a total of 1458 non-redundant proteins in eluted fractions from ds_r8oxoG:dC_Biot (Supplementary Table S1).

We identified a total of 1202 non-redundant proteins in eluted fractions from ds_rF:dC_Biot. Finally, proteomic analysis assigned a total of 1474 non-redundant proteins in eluted fractions from ds_rG:dC_Biot (Supplementary Fig. S2A and dataset identifier PXD027252). About 1173 proteins were common to all samples, whereas 9, 256 and 11 components were shared between ds_r8oxoG:dC_Biot and ds_rF:dC_Biot, ds_r8oxoG:dC_Biot and ds_rG:dC_Biot, and ds_rF:dC_Biot and ds_rG:dC_Biot, respectively (Supplementary Fig. S2A).

Further, we functionally characterized both the ds_r8oxoG:dC_Biot and ds_rF:dC_Biot interactomes querying several functional and metabolic databases (Supplementary Fig. S2B–D). Among the most enriched terms, for both protein groups, we found *mRNA metabolic process* (35.17% and 57.95%, respectively), followed by *proteins involved in the metabolism of RNA* (17.93% and 29.55%, respectively). Although to a much lesser extent, the common term *translation* was also present (2.07% and 3.41%, respectively). Notably, several eluted proteins, including AUF1, PCBP1, Top1, MPG, and others, are mostly involved in DNA repair and RNA metabolism (Cerritelli et al., 2020; Jobert and Nilsen, 2014; Liu et al., 2020; Mohanty et al., 2021; Promonet et al., 2020; Sidali et al., 2021).

To demonstrate the specificity of the used approach, we tested the collected fractions for the presence of APE1, since this protein was specifically identified only in the proteomic list of the ds_rF:dC binding proteins (see dataset identifier PXD027252). Through Western blot analysis, we confirmed the presence of APE1 in the samples obtained on elution with 300 m*M*, 400 m*M* and, to a lesser extent, with 600 m*M* NaCl (lanes 2-3-4) (Supplementary Fig. S1B). Moreover, since APE1 is the only enzyme able to efficiently cleave the ds_rF:dC, as we have previously demonstrated (Malfatti et al., 2017), we analyzed the same samples through an endonuclease assay to evaluate the APE1 activity on ds_rF:dC.

We incubated all the eluted fractions with the ds_rF:dC oligonucleotide and we performed the endonuclease assay analysis, comparing the signal of the uncleaved substrate *versus* the cleaved product. In Supplementary Figure S1C, the obtained data clearly demonstrated that the major specific APE1 endonuclease activity was detectable in samples eluted at the concentration of 300 m*M* NaCl (lane 3) and, to a lesser extent, of 400 m*M* NaCl (lane 4). These data confirmed the specificity of the enrichment procedure we used to capture proteins recognizing the different lesions.

AUF1 binds DNA-embedded 8-oxo-guanosine in vitro

In proteomic data, we found several putative 8-oxo-guanosine-binding proteins known to be involved in DNA repair and RNA metabolism, including AUF1, PCBP1, Top1, and MPG (dataset identifier PXD027252, Supplementary Figs. S1 and S2). Among them, we focused our attention on AUF1. Indeed, this protein, also named hnRNP D, is a ribonucleoprotein (Moore et al., 2014) that specifically recognizes oxidized mRNA (Hayakawa et al., 2010; Ishii and Sekiguchi, 2019; Ishii et al., 2018; Ishii et al., 2015). Unfortunately, the authors did not prove any specific activity of AUF1 on oxidized mRNA (Ishii and Sekiguchi, 2019).

Therefore, we investigated AUF1 ability to recognize the ds_r8oxoG:dC oligonucleotide through Western blotting experiments performed on protein fractions captured by affinity chromatography. When we analyzed fractions captured with the ds_r8oxoG:dC_Biot oligonucleotide (Fig. 2B), Western blot analysis clearly confirmed the enriched presence of AUF1 in these samples, and particularly in that eluted with 300 m*M* NaCl, compared with other DNA probes (Fig. 2C).

A band smearing phenomenon hampering accurate AUF1 mass measurement was also observed for NCE, which did not occur for the earlier mentioned fractions. This was associated with the different amount of AUF1 loaded into gel lanes in the different cases and/or the possible, concomitant presence of ribonucleoprotein isoforms (p45, p43, p42, and p40) in NCE, which are generated after alternative splicing events. A careful inspection of the gel image revealed that the AUF1 isoform enriched by affinity chromatography was the one having the highest mass value, probably p45, which was also the protein form we used in the subsequent *in vitro* assays.

To gather more insights into the possible role of AUF1 in recognizing 8-oxo-guanosine, we used a purified, recombinant AUF1 (rAUF1) obtained from *Escherichia coli*. Purified rAUF1 was quantified by using a bovine serum albumin (BSA) linear range titration curve, as shown in Supplementary Figure S2E. Then, we investigated the *in vitro* ability of rAUF1 in binding to ds_r8oxoG:dC. On incubation of rAUF1 with the ds_r8oxoG:dC oligonucleotide, and after ultraviolet (UV)-crosslinking, samples were separated onto a denaturing gel and the signal of the protein-DNA complex was detected.

As shown in Figure 2D, rAUF1 was able to specifically bind to the DNA oligonucleotide containing the 8-oxo-guanosine site (lanes from 6 to 8). The specificity of the binding was confirmed by comparing the signal obtained with the ds_r8oxoG:dC to that of the ds_dG:dC oligonucleotide containing the unmodified dGMP site as a control (Fig. 2A), on which rAUF1 showed an evident, lower binding ability, as expected (lanes from 2 to 4) (Fig. 2D). Then, we performed an electrophoretic mobility shift analysis (EMSA) experiment to detect the ability of rAUF1 to bind to the ds_r8oxoG:dC probe and to generate stable protein-DNA complexes under native conditions (Fig. 2E).

Again, the experiment was performed using both the ds_r8oxoG:dC oligonucleotide and the ds_dG:dC oligonucleotide, as a negative control. The retarded bands, observed

when rAUF1 was incubated with ds_r8oxoG:dC, confirmed the generation of a stable protein-DNA complex formed in a dose-response dependent manner (lanes 5 and 6). On the contrary, no signals were detected when rAUF1 was incubated with the ds_dG:dC oligonucleotide control (lanes 2 and 3). All these data confirmed the ability of AUF1 to specifically bind to the 8-oxo-guanosine site embedded in DNA.

AUF1 stimulates APE1-binding and endoribonuclease activity on 8-oxo-guanosine in vitro

We then investigated the possible activity of AUF1 in contributing to the processing of the 8-oxo-guanosine by APE1. First, we performed EMSA to investigate whether the presence of AUF1 could modulate APE1 ability to bind to the ds_r8oxoG:dC probe. The experimental setting consisted of a pre-incubation of the oligonucleotide with rAUF1 protein, followed by the addition of rAPE1. As shown in Figure 2F, rAUF1 alone (lanes 2 and 3) was able to bind the 8-oxo-guanosine site in a dose-dependent manner (the complex is indicated by one asterisk), confirming previous data. On the contrary, rAPE1 alone was able to bind the oligonucleotides with a weak activity, visible as a faint band (lanes 5 and 6, the complex is indicated by two or three asterisks).

Interestingly, when both proteins were co-incubated together with the probe, we observed an increase in the oligonucleotide-protein complex formation, marked by two and three asterisks and corresponding to the APE1-DNA bound complexes (compare lanes 4 with 7 and 8; lane 5 with 9 and 10; lane 6 with 11 and 12). Quantification of the intensity of each retarded complex is reported as histograms on the right of Figure 2F. These data suggest a role of AUF1 in stabilizing the APE1-DNA complex formation on the ds_r8oxoG:dC oligonucleotide.

Endonuclease assays were then performed to evaluate a possible stimulatory effect exerted by AUF1 on the APE1 enzymatic activity on ds_r8oxoG:dC (Fig. 2G). Experiments were performed under the same experimental conditions reported in Figure 2F. First, we observed that AUF1, despite its ability to bind 8-oxo-guanosine, was unable to exert any cleavage activity *per se* (lane 2). In parallel, APE1 alone, as already published (Malfatti et al., 2017), was able to weakly process the oligo with low efficiency, reaching a plateau at about 13% of processed substrate (lane 3).

Remarkably, when APE1 was pre-incubated with AUF1, its cleavage activity on ds_r8oxoG:dC increased up to 49% (lane 4). In this context, we also used two APE1 mutants previously characterized in our laboratory, namely $APE1^{N\Delta33}$ that lacks the first 33 amino acids at the protein N-terminus (Fantini et al., 2010; Poletto et al., 2013), and the dead endonuclease mutant $APE1^{E96A}$ (Barnes et al., 2009; He et al., 2014). Like the wild-type counterpart, $APE1^{N\Delta33}$ preserved the same ability to cleave 8-oxo-guanosine (lane 5), showing an increased endonuclease activity in the presence of AUF1 (lane 6). Contrarily, although as expected, $APE1^{E96A}$ was unable to cleave 8-oxo-guanosine, also in the presence of AUF1, confirming that the increased processing activity exerted after AUF1 co-incubation only affects the APE1 endonuclease activity.

Interestingly, in correspondence to the bottom of the wells of the denaturing gel where the AUF1-containing samples were loaded, we observed the formation of intense signals presumably due to a hefty DNA-protein covalent complex unable to properly enter the gel matrix (Fig. 2G). For this reason, on protein incubation with oligonucleotides as cited earlier, we completed the reactions by treating the samples with proteinase K to allow protein degradation; then, we performed gel separation. As shown in Figure 2H, the band corresponding to the large DNA-protein complex was not present anymore, whereas a clear increase in the oligonucleotide product formation on reaction with APE1 was detectable in an AUF1-dependent manner.

Earlier mentioned data demonstrated that AUF1 increases the ability of APE1 to bind to the ds_r8oxoG:dC oligonucleotide, and simultaneously is able to stimulate the processing activity of APE1, which is independent of the first 33 N-terminal residues. Moreover, experiments with proteinase K clearly showed that the formation of an intermediate covalent AUF1-DNA complex occurs during the enzymatic reaction, which will deserve further attention.

Characterization of the interaction between APE1 and AUF1

To further investigate the functional relationship existing between APE1 and AUF1, we tested whether these two proteins were able to physically interact using glutathione S-transferase (GST)-pulldown and proximity ligation analysis (PLA)-assays. First, we verified the APE1–AUF1 interaction *in vitro* by using recombinant purified APE1 proteins (the wild type and NΔ33 deletion mutant), tagged with GST (rGST-APE1), and rAUF1 protein (His-tagged).

We performed a GST-pulldown assay (Fig. 3A) in which rGST-APE1 was incubated with rAUF1. As a negative control of the interaction, rAUF1 was also incubated with recombinant GST alone. As shown in Figure 3A, the increased AUF1 signal, compared with GST alone, confirmed the occurrence of a specific interaction between AUF1, $APE1^{WT}$, and the $APE1^{N\Delta33}$ deletion mutant (lanes 5 and 6, respectively). Then, we checked the occurrence of the interaction in HeLa cells through PLA, which allows the detection of the proximity of two proteins within a 40 nm of distance (Alam, 2018).

Figure 3B shows a representative PLA image between APE1 and AUF1 under basal conditions. The considerable number of red dots indicated the occurrence of APE1–AUF1 physical proximity in HeLa cells. The number of dots was quantified to estimate the amount of protein-protein interaction *per* cell (Fig. 3B) in comparison to negative control, in which the APE1 antibody was omitted in the PLA experiment. The plot in Figure 3C shows the quantitative difference in the number of dots after comparing results from both experimental conditions. Notably, the median of the negative control was around 3 dots *per* cell, compared with the APE1–AUF1 counterpart that was equal to 52.

To confirm these data, another PLA experiment was performed in HeLa cells on silencing or overexpression of the AUF1 protein, through specific siRNA and AUF-expressing plasmid, respectively (Fig. 3D–I). First, cells were transfected by using specific siRNA directed to the AUF1 mRNA. The AUF1 protein silencing was evaluated by using Western blot after 48 h of transfection. The silenced for AUF1 (siAUF1) condition was compared with both negative silencing controls, namely Mock, corresponding to non-transfected HeLa cells, and siSCR, corresponding to cells transfected with the non-targeting siRNA (Fig. 3D).

As observed in the Western blot panels, the AUF1 protein levels decrease of about 70% on siRNA transfection, compared with siSCR. Corresponding PLA analyses were

performed as described earlier. In Figure 3E, siSCR cells showed a higher number of PLA dots, when compared with siAUF1 cells, in which the amount of PLA dots was greatly reduced. PLA dots were quantified, and their number was compared between the two conditions.

The plot shown in Figure 3F clearly reveals that the APE1–AUF1 interaction was significantly reduced after the silencing of AUF1, reaching almost a six-fold decrease. In parallel, as a confirmatory experiment, HeLa cells were transfected with a plasmid expressing the FLAG-tagged AUF1 to overexpress the AUF1 protein. On 48 h of transfection, AUF1 levels were analyzed through Western blotting to confirm the AUF1 overexpression and its signal was compared with the Empty condition, which was obtained by cell transfection with the empty-vector plasmid (Fig. 3G).

Then, corresponding cells were analyzed through PLA as described earlier. As shown in Figure 3H, the number of red dots was significantly increased after overexpression of the FLAG-tagged AUF1 protein. Data were also confirmed by performing PLA analysis by using the APE1 and FLAG antibodies (Supplementary Fig. S3). PLA dots were quantified, and their number was compared with the Empty condition.

The plot, represented in Figure 3I, clearly shows that the APE1–AUF1 interaction was significantly increased after the overexpression of FLAG-tagged AUF1, reaching more than a twofold increase in the FLAG-AUF1 cells, compared with the Empty counterpart.

Taken together, these data confirmed that APE1 directly interacts with AUF1 and that the interaction does not involve the N-terminal 33 residues of APE1, supporting the previous enzymatic data.

AUF1 interaction with APE1 is modulated by H_2O_2- and $KBrO_3$-treatments and protects from oxidation-induced damage

As already mentioned, both APE1 and AUF1 are involved in modulating cellular response to oxidative stress through different mechanisms (Daviet et al., 2007; Ishchenko et al., 2006; Ishii et al., 2015). This prompted us to explore the role of the AUF1–APE1 interaction during early times of oxidative stress conditions obtained by treatment with H_2O_2 or $KBrO_3$.

We first defined proper treatments to have an acute oxidative stress condition, avoiding secondary effects due to cell death induced by H_2O_2 treatment. The optimal dosage of H_2O_2-induced DNA damage was measured by evaluating the extent of the γH2AX foci formation by immunofluorescence analysis (Supplementary Fig. S4A, B), as well as by Western blot (Supplementary Fig. S4C), and by measuring the Prxs-oxidation status through Western blotting (Supplementary Fig. S4D) (Sies, 2017), and its effect on cell viability by metabolic analysis (Supplementary Fig. S4E).

Specifically, H_2O_2 treatment for 15 min with 500 μM in a serum-free medium represented a good compromise between the induction of a prooxidant status and a mild effect in terms of DNA damage. In the case of $KBrO_3$ treatment, according to literature data (Amouroux et al., 2010) and viability assays (data not shown), we chose a treatment with 40 mM $KBrO_3$ for 35 min, in a serum-free medium, to induce a mild DNA oxidative damage.

Then, we tested the effect of H_2O_2 and $KBrO_3$ treatments on the interaction between APE1 and AUF1 by performing a PLA analysis on treated cells; for this purpose, the number of red dots was counted and compared with that of untreated cells. As shown in the representative PLA images (Fig. 4A), the interaction between APE1 and AUF1 was significantly decreased after oxidative stress. Specifically, the number of red dots *per* cell underwent $\sim$74% reduction, when compared with the PLA dots counted in untreated cells (Fig. 4B), considering a median of 42 dots *per* cell in untreated cells *versus* 11 dots *per* cell in H_2O_2-treated cells. Similar results were obtained with $KBrO_3$ treatment (Fig. 4C), in which the interaction between APE1 and AUF1 was significantly decreased. Specifically, the number of red dots *per* cell underwent approximately an 88% reduction, when compared with PLA dots counted in untreated cells (Fig. 4D).

FIG. 3. AUF1 interacts with APE1. (A) GST-pulldown of recombinant GST, GST-APE1^{WT} and GST-APE1$^{N\Delta 33}$ with recombinant AUF1. Immunoblotting analysis of the input and eluted fractions shows the amount of AUF1 and GST (IB: AUF1 and IB: GST). Below the Western blot *panel*, the signal of AUF1, normalized to the corresponding GST protein signal, is expressed as arbitrary units ($n=2$). **(B)** HeLa cells were seeded on a glass coverslip, and PLA-Cy3 reaction was carried out using anti-APE1 and anti-AUF1 antibodies (*red* spots). AUF1 expression was detected by using the AUF1-488 antibody (*green*). Nuclei were visualized with DAPI (*blue*). Scale bars are indicated in the merge *panel*. **(C)** *Dot* plot accounting for the number of PLA *dots per* cell of randomly selected cells. Data were collected from three independent biological replicas. **(D)** Representative immunoblotting analysis on WCE of HeLa cells shows the amount of AUF1 on different conditions including Mock, corresponding to no transfected cells, siSCR, corresponding to cells transfected for 48 h with siRNA control, and siAUF1, corresponding to cells transfected for 48 h with siRNA directed *versus* AUF1. On the *left* side of each *panel*, specific antibodies used in the immunoblotting are indicated. Tubulin was used to normalize AUF1 levels. **(E)** HeLa cells were seeded on a glass coverslip and treated with siSCR and siAUF1 shRNAs for 48 h. The PLA-Cy3 reaction was carried out using anti-APE1 and anti-AUF1 antibodies (*red* spots). AUF1 expression was detected by using the AUF1-488 antibody (*green*). Nuclei were visualized with DAPI (*blue*). Scale bars are indicated in the merge *panel*. The *yellow arrow* points out to silenced cells for AUF1. **(F)** *Dot* plot accounting for the number of PLA *dots per* cell. Data were collected from three independent biological replicas. **(G)** Representative immunoblotting analysis on WCE of HeLa cells shows AUF1 levels in Empty, corresponding to cells transfected for 48 h with plasmid control, and FLAG-AUF1, corresponding to cells transfected for 48 h with plasmids overexpressing FLAG-AUF1. On the *left* side of each *panel*, the specific antibodies used in the immunoblotting are indicated. Tubulin was used to normalize AUF1 levels. **(H)** The representative PLA image for HeLa cells treated with FLAG-AUF1 overexpressing plasmid for 48 h. The PLA-Cy3 reaction was carried out using anti-APE1 and anti-AUF1 antibodies (*red* spots). AUF1 expression was detected by using the AUF1-488 antibody (*green*). Nuclei were visualized with DAPI (*blue*). Scale bars are indicated in the merge *panel*. **(I)** *Dot* plot accounting for the number of PLA *dots per* cell. Data were collected from three independent biological replicas. GST, glutathione S-transferase; PLA, proximity ligation analysis; siAUF1, silenced for AUF1; WCE, whole cell extracts.

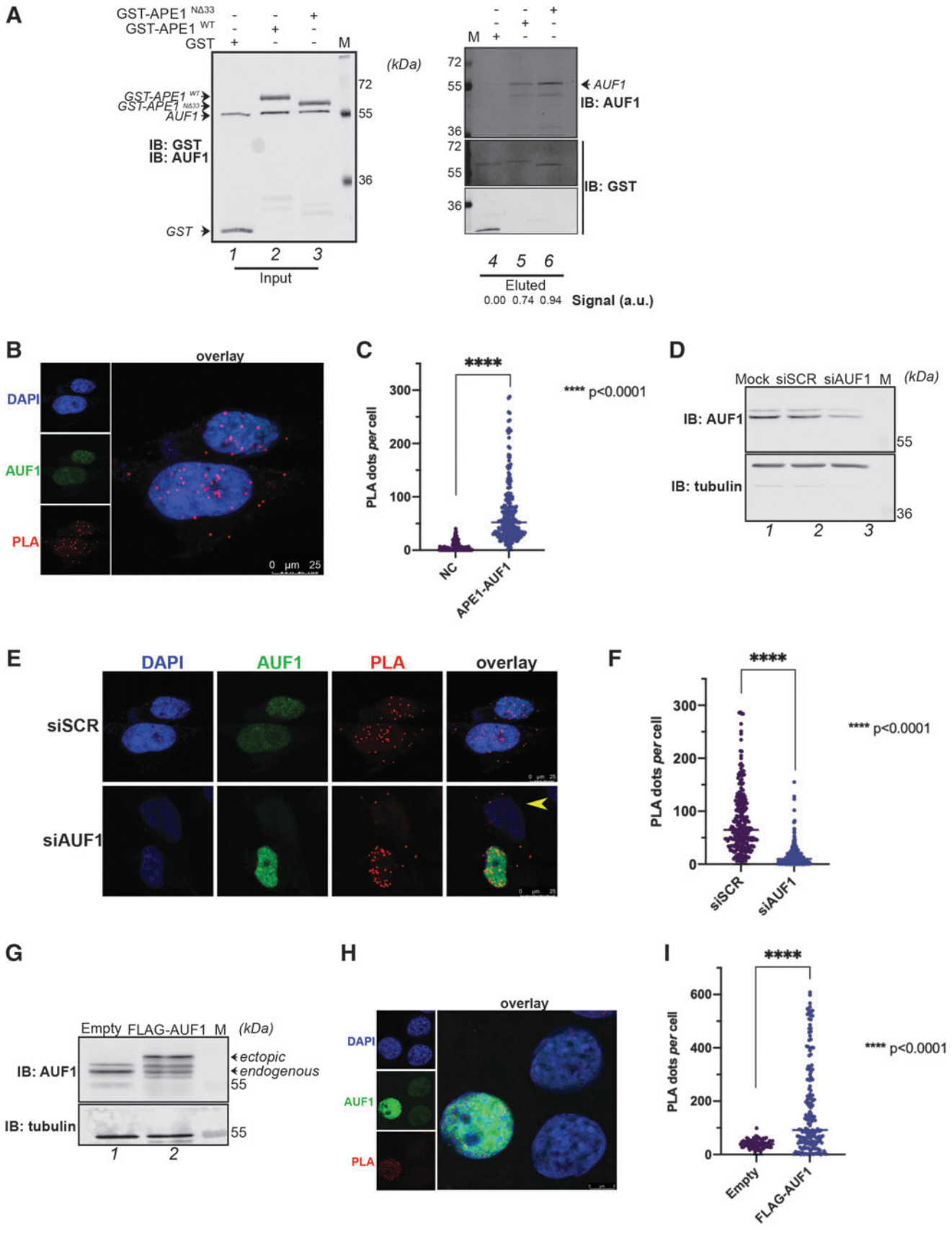
A
GST-APE1 NΔ33
GST-APE1 WT
GST
M
(kDa)
72
55
36
GST-APE1 WT
GST-APE1 NΔ33
AUF1
IB: GST
IB: AUF1
GST
1 2 3
Input
AUF1
IB: AUF1
IB: GST
4 5 6
Eluted
0.00 0.74 0.94 Signal (a.u.)
B
overlay
DAPI
AUF1
PLA
0 µm 25
C
****
**** p<0.0001
PLA dots per cell
300
200
100
0
NC
APE1-AUF1
D
Mock siSCR siAUF1 M (kDa)
IB: AUF1
IB: tubulin
55
36
1 2 3
E
DAPI
AUF1
PLA
overlay
siSCR
siAUF1
F
****
**** p<0.0001
PLA dots per cell
300
200
100
0
siSCR
siAUF1
G
Empty FLAG-AUF1 M (kDa)
IB: AUF1
IB: tubulin
ectopic
endogenous
55
55
1 2
H
overlay
DAPI
AUF1
PLA
I
****
**** p<0.0001
PLA dots per cell
600
400
200
0
Empty
FLAG-AUF1

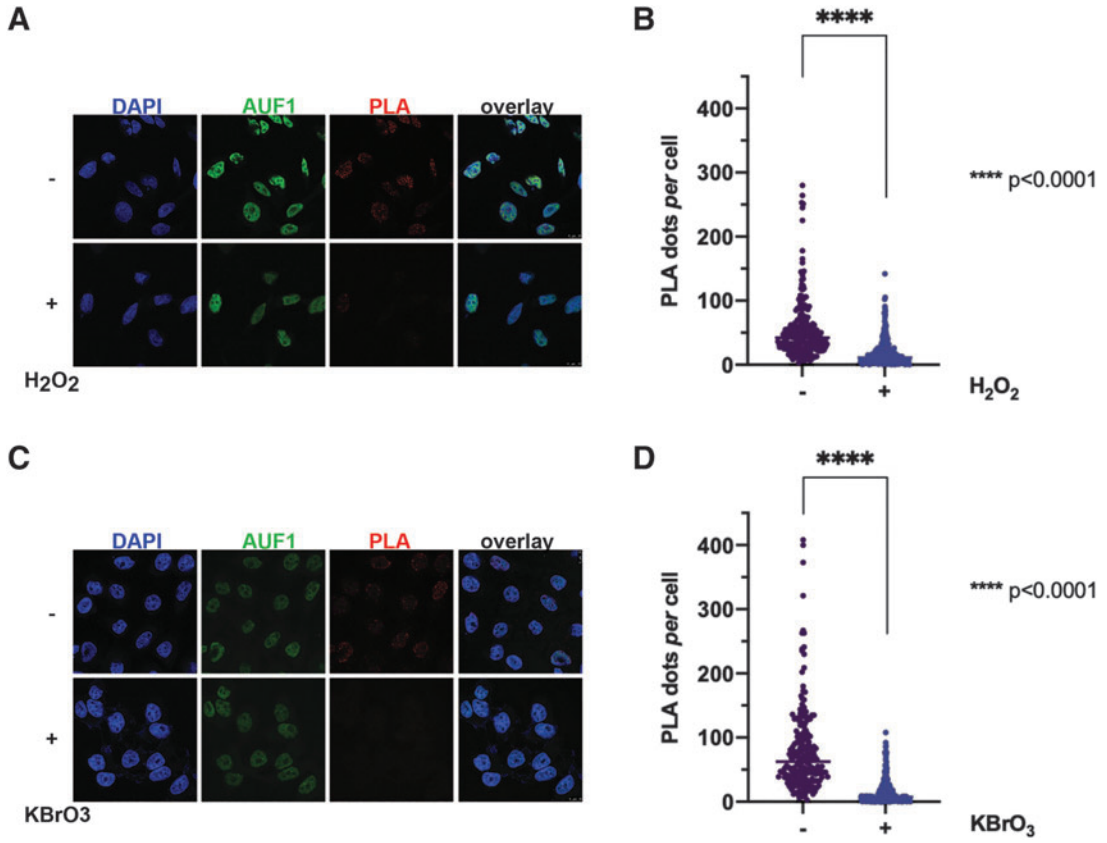

FIG. 4. The APE1–AUF1 interaction is modulated by oxidative stress. (A) PLA analysis on HeLa cells untreated and treated with 500 μM H_2O_2 for 15 min. The PLA-Cy3 reaction was carried out using anti-APE1 and anti-AUF1 antibodies (*red* spots). AUF1 expression was detected by using the AUF1-488 antibody (*green*). Nuclei were visualized with DAPI (*blue*). Scale bars are indicated in the merge *panel*. **(B)** Data reported in the histogram account for the number of PLA *dots per* cell. Data were collected from three independent biological replicas. **(C)** PLA analysis on HeLa cells untreated and treated with 40 m*M* $KBrO_3$ for 35 min. The PLA-Cy3 reaction was carried out using anti-APE1 and anti-AUF1 antibodies (*red* spots). AUF1 expression was detected by using the AUF1-488 antibody (*green*). Nuclei were visualized with DAPI (*blue*). Scale bars are indicated in the merge *panel*. **(D)** Data reported in the histogram account for the number of PLA *dots per* cell. Data were collected from three independent biological replicas. $^{****}p < 0.0001$.

AUF1 and APE1 cooperate in protecting cells from oxidation-induced DNA damage accumulation

We evaluated whether AUF1 and APE1 are in synthetic lethality relationships with respect to H_2O_2 and $KBrO_3$ treatments. Thus, we treated HeLa cells, previously depleted of the APE1 and AUF1 proteins, with 500 μM of H_2O_2 for 15 min, or 40 m*M* of $KBrO_3$ for 35 min, in a serum-free medium. A Western blot analysis confirmed the decrease of the protein levels on 48 h of transfection of both APE1 and AUF1 after siRNA treatment and compared with the transfected control siSCR cells (Fig. 5A), as well as the increase of the $PrxSO_3$ levels after H_2O_2 treatment (Supplementary Fig. S5).

FIG. 5. Genomic stability depends on the APE1–AUF1 interaction following oxidative stress. (A) Representative APE1 and AUF1 immunoblotting analysis on WCE of transfected HeLa cells. Revert700 staining was used as a protein normalizer. Below, the histogram indicates the levels of APE1 and AUF1, normalized on Revert700, in silenced cells, normalized to siSCR. **(B)** Violin plot showing the amount of AP sites measured on transfected HeLa cells. Data were collected from three independent biological replicas. $^{*}p = 0.01$; $^{***}p = 0.0002$. **(C)** Violin plot reports the amount of AP sites measured on transfected HeLa cells upon H_2O_2 and $KBrO_3$. Data were collected from three independent biological replicas. $^{*}p < 0.05$; $^{****}p < 0.0001$. **(D)** Representative images for transfected HeLa cells on treatment with 500 μM H_2O_2 for 15 min for detection of γH2AX foci. The amount of γH2AX foci in untreated cells was also analyzed for comparison. Nuclei were visualized with DAPI (*blue*). Scale bars are indicated. **(E)** Data reported in the box plot account for the number of γH2AX foci intensity *per* cell of randomly selected cells. Data were collected from three independent biological replicas. Individual values are shown with mean ± SD. $^{****}p < 0.0001$. **(F)** Representative images for transfected HeLa cells on treatment with 500 μM H_2O_2 for 15 min for analysis of DNA comet. Untreated cells were also analyzed for comparison. **(G)** Data reported in the box plot account for the number of olive tail moments *per* cell of randomly selected cells. Data were collected from two independent biological replicas. Individual values are shown with mean ± SD. $^{*}p = 0.0112$; $^{****}p < 0.0001$. SD, standard deviation.

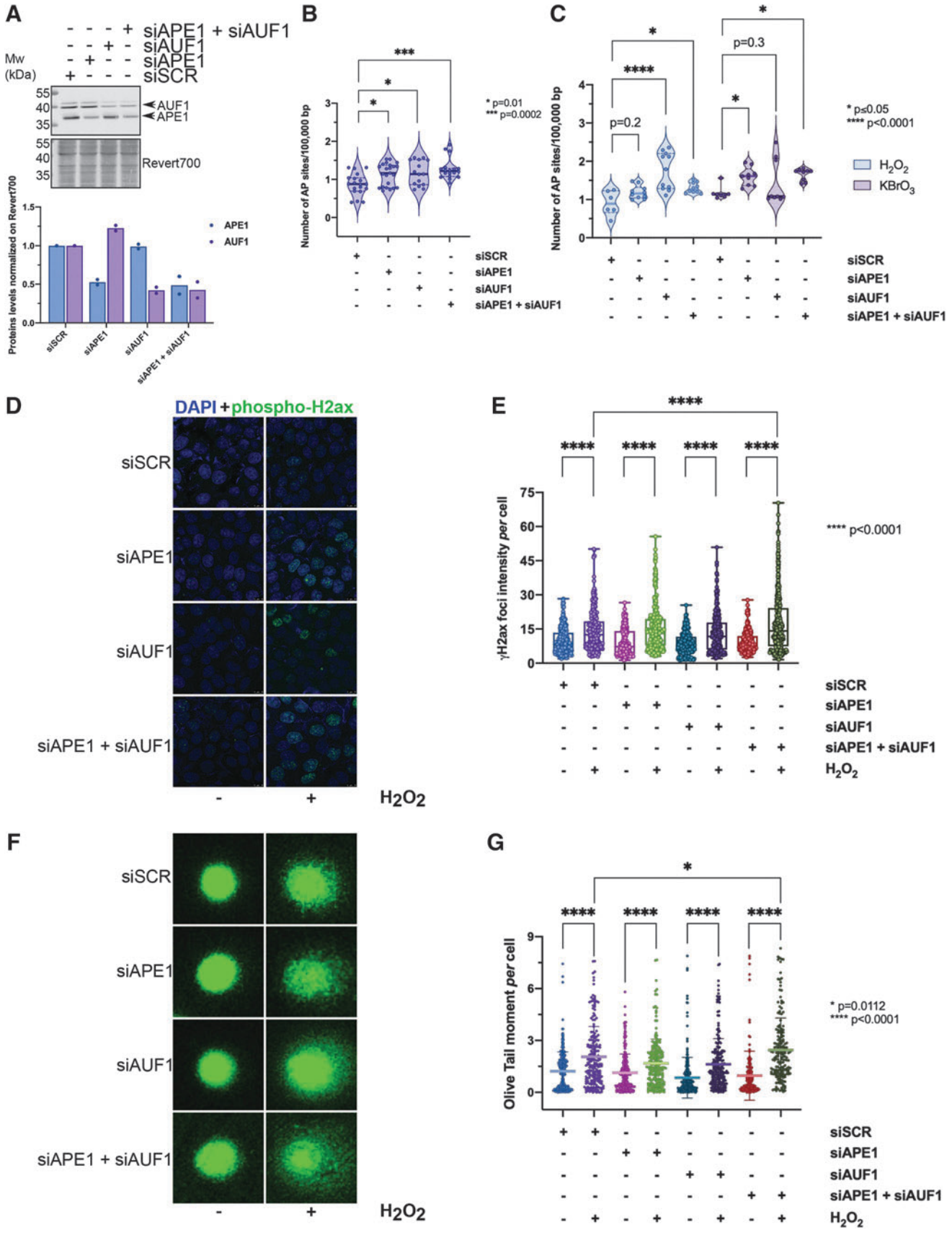
A
siAPE1 + siAUF1
siAUF1
siAPE1
siSCR
Mw
(kDa)
55
40
35
AUF1
APE1
Revert700
Proteins levels normalized on Revert700
APE1
AUF1
siSCR
siAPE1
siAUF1
siAPE1 + siAUF1
B
Number of AP sites/100,000 bp
* p=0.01
*** p=0.0002
C
Number of AP sites/100,000 bp
p=0.2
p=0.3
* p≤0.05
**** p<0.0001
H2O2
KBrO3
D
DAPI + phospho-H2ax
siSCR
siAPE1
siAUF1
siAPE1 + siAUF1
H2O2
E
γH2ax foci intensity per cell
**** p<0.0001
F
siSCR
siAPE1
siAUF1
siAPE1 + siAUF1
H2O2
G
Olive Tail moment per cell
* p=0.0112
**** p<0.0001

We then evaluated whether the AUF1/APE1 expression plays a role in controlling genome stability. The product generated during the DNA repair process of oxidized bases is represented by the loss of the base, through hydrolysis of the N-glycosidic bond, leading to the formation of an abasic site (Krokan and Bjørås, 2013); this site is then processed by APE1 into a single-strand break that will be completely repaired by additional BER enzymes. Therefore, we investigated the impact of APE1- and/or AUF1-depletion on the AP-generation under basal conditions (Fig. 5B) and on oxidative stressors including H_2O_2 and $KBrO_3$ (Fig. 5C) by measuring the amount of abasic sites *per* 100,000 base pairs.

By using an ELISA assay based on the reaction between the aldehyde-reactive probe substrate and the aldehyde group present on the open ring form of the AP-sites, we quantified the number of AP-sites on 100,000 bp of genomic DNA extracted from HeLa cells, which were previously silenced for APE1 (siAPE1) and AUF1 proteins. Untreated cells, independently siAPE1 or siAUF1, showed a slight, although significant, increase of AP-sites, when compared with siSCR, under basal conditions. Interestingly, a significant increase of AP-sites was observed when we combined the depletion of APE1 with AUF1 (Fig. 5B).

Remarkably, the increase of AP-sites was more relevant when cells were exposed to H_2O_2 and, even though to a lesser extent, when exposed to $KBrO_3$, suggesting that the concomitant knock-down of both the APE1 and AUF1 proteins, and the exposition to an oxidative stressor, led the cells to an accumulation of DNA damage (Fig. 5C). We then evaluated the effect of APE1/AUF1 depletion on DNA double-strand breaks formation through the detection and quantification of the phosphorylated Ser139 of the histone variant H2AX (γH2AX) (Mah et al., 2010).

By monitoring the fluorescence of γH2AX in all silencing conditions, under basal as well as on H_2O_2 treatment, we observed an increase of the intensity of γH2AX foci *per* cell area on oxidative conditions (Fig. 5D and Supplementary Fig. S6). The quantification of the foci intensity *per* cell confirmed this observation, defining a statistically significant increase of γH2AX foci in the H_2O_2-treated cells on combined depletion of both APE1 and AUF1 (siAPE1+siAUF1), compared with H_2O_2-treated siSCR cells (Fig. 5E).

Further, DNA double- and single-strand breaks levels, as well as that of alkali-sensitive label sites, such as abasic sites, were detected by exploiting the alkaline comet analysis. As shown in the representative single comet cell images (Fig. 5F), the typical DNA comet was apparent on H_2O_2 treatment, as expected. By measuring the olive tail moment of a cohort of cells in the eight conditions, a significantly higher rate of DNA damage accumulation was observed in all the H_2O_2-treated cells. Again, the combined depletion of both APE1 and AUF1 exhibited a higher olive tail moment compared with H_2O_2-treated siSCR alone (Fig. 5G).

To understand whether APE1 and AUF1 are in a synthetic lethality relationship, we performed colony formation assays to measure the effect of siRNA-mediated APE1/AUF1-depletion on cell growth. Specifically, we counted the number of colonies grown over a period of 10 days. As shown in Figure S7A, no significant difference in cell growth was observed. Moreover, the effect of H_2O_2-treatment on cell viability was evaluated with the [3-(4,5-dimethylthiazol-2-yl)-5-(3-carboxymethoxyphenyl)-2-(4-sulfophenyl)-2H-tetrazolium, inner salt assay and compared with the control. Data shown in Figure S7B demonstrated that not only depletion of APE1 but also that of AUF1 slightly sensitized cells to H_2O_2 treatment. The concomitant depletion of APE1 and AUF1 exerted a slight, although significant, effect on cell sensitization to treatment with H_2O_2.

Altogether, these data confirmed the well-known relevance of APE1 in the processing of damaged DNA, after cell exposure to oxidative stress by hydrogen peroxide. Remarkably, our data show that AUF1 significantly contributes to the maintenance of genome stability against oxidative stress (Ishii et al., 2015) in synergism with APE1.

AUF1 and APE1 are involved in DNA:RNA hybrids resolution

Since 8-oxo-guanosine embedded in DNA represents a type of D:R hybrid, we inspected the role of APE1 and AUF1, as well as their interaction, in affecting generation and/or processing of D:R hybrids. As previously stated, RNase H1 is the main enzyme responsible for the resolution of D:R hybrids, such as R-loops, which are formed during several biological processes, including DNA replication. In particular, overexpression of this protein should promote the resolution of the R-loop in the cell (Lockhart et al., 2019).

Based on these premises, we first measured the effect of overexpressing FLAG-RNase H1 in HeLa cells on the APE1–AUF1 interaction through PLA analysis. PLA representative images clearly showed the decrease of the APE1–AUF1 interaction on transient overexpression of RNase H1 (Fig. 6A), which was statistically significant when evaluating the number of red dots and accounted for about 60% (Fig. 6B).

We further investigated the existence of a possible role of both proteins in the resolution of D:R hybrids. By using the previous experimental setup of HeLa cells silenced for the APE1 and AUF1 proteins, separately or in combination, we extracted and purified their genomic DNA and quantified the D:R hybrids formation through dot blot assay and by using the S9.6 antibody, a clone detecting D:R hybrids (Fig. 6C, D). Immunoblot with the S9.6 antibody was used to quantify the amount of R-loops relative to the signal obtained on incubation with a specific antibody recognizing the ssDNA amount, as a loading control (Fig. 6C) (Ramirez et al., 2021).

As shown in Figure 6D, the R-loops levels were remarkably increased when APE1 was downregulated, both separately and in combination with AUF1. Indeed, a 2-fold increase was observed on depletion of APE1 and a 1.6-fold increase on depletion of both APE1 and AUF1, in comparison to siSCR cells. Although not statistically significant, the knock-down of AUF1 alone increased, by about 36%, the amount of R-loop formation within cells. We then tested the physical presence of both proteins on R-loops by using a D:R immunoprecipitation (DRIP) assay, as described in the experimental section.

The DRIP assay represents an unbiased approach that is useful for the isolation of D:R hybrids, including R-loops, and for the identification of their associated proteins (Cristini et al., 2018). Specifically, we first isolated nuclei from cultured cells and performed chromatin extraction and sonication; then, the S9.6 antibody was used for the recognition of D:R structures and their immunoprecipitation. Finally, after Western blot analysis, we detected and identified R-loop-binding proteins; results are shown in Figure 6E.

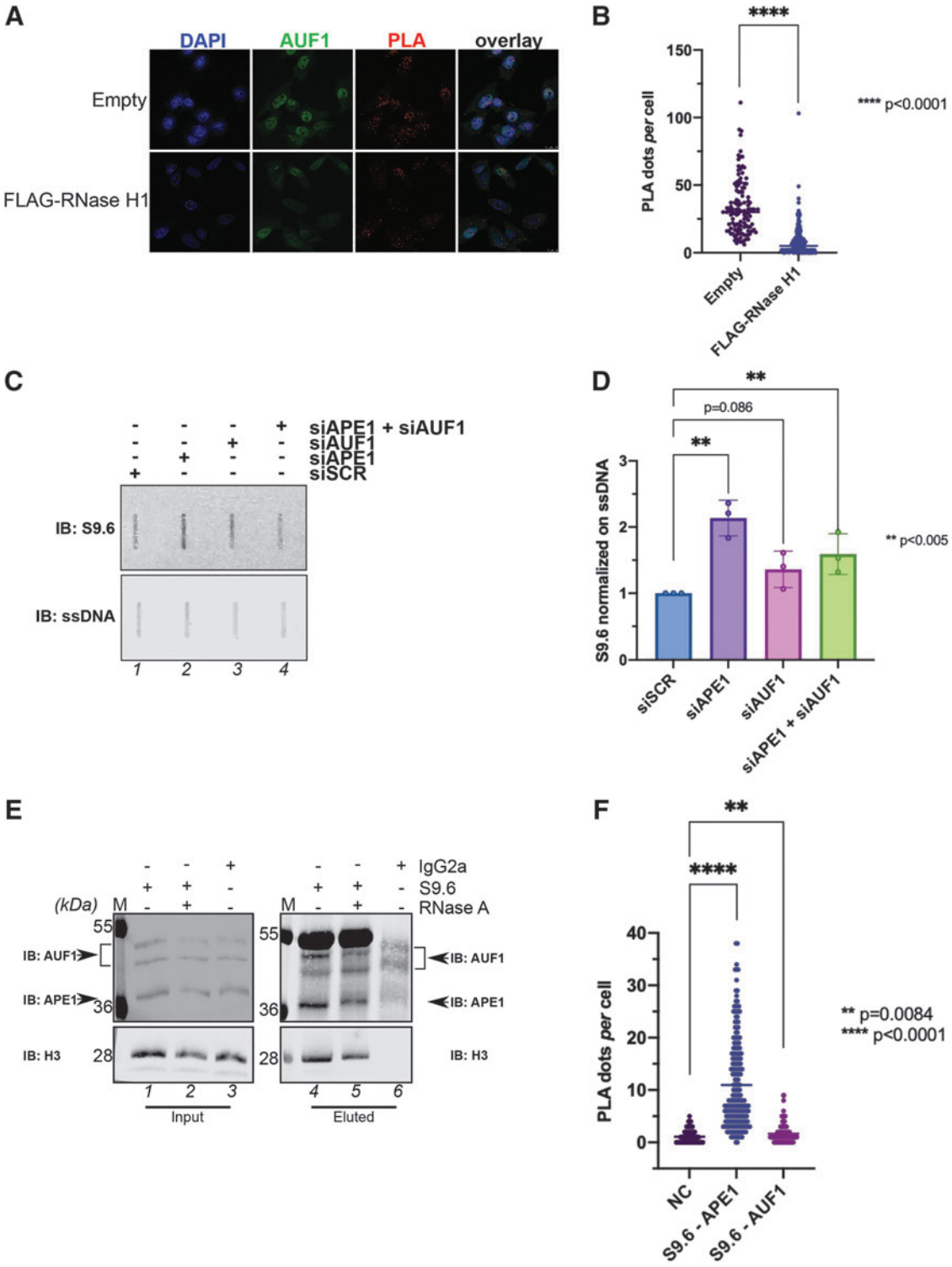

FIG. 6. Both APE1 and AUF1 proteins are involved in D:R hybrids resolution. **(A)** PLA analysis on HeLa cells transfected with a plasmid overexpressing FLAG-RNase H1 or an empty plasmid (control) for 48 h. The PLA-Cy3 reaction was carried out using anti-APE1 and anti-AUF1 antibodies (*red* spots). AUF1 expression was detected by using the AUF1-488 antibody (*green*). Nuclei were visualized with DAPI (*blue*). Scale bars are indicated in the merge *panel*. **(B)** Data reported in the *dot* plot account for the number of PLA *dots per* cell. Data were collected from three independent biological replicas. $****p < 0.0001$. **(C)** *Dot* blot analysis for S9.6 antibody on genomic DNA from transfected HeLa cells. ssDNA was used as a normalizer. **(D)** Data reported in the histogram show the S9.6 level detected by *dot* blot analysis and normalized on ssDNA. Data were collected from three independent biological replicas. Individual values are shown with mean ± SD. $**p < 0.005$. **(E)** DRIP analysis followed by Western blot analysis of the input and eluted fractions shows the amount of AUF1 and APE1 (IB: AUF1 and IB: APE1). Histone H3 was used as a normalizer (IB: H3). Data were collected from two independent biological replicas. **(F)** Data reported in the histogram account for the number of PLA *dots per* cell. Data were collected from three independent biological replicas. $**p = 0.0084$; $****p < 0.0001$. D:R, DNA:RNA; DRIP, D:R immunoprecipitation.

It was evident that APE1 and AUF1 were immunoprecipitated after the use of the S9.6 antibody (lanes 4–5), while they were absent when the IgG2a control antibody was used (lane 6), thus confirming the specificity of the interaction. Treatment with RNase A did not interfere with the APE1 and AUF1 binding to the R-loop, as expected (lane 5). To confirm the physical presence of APE1 and AUF1 on the DNA:RNA hybrids, a PLA analysis was also performed (Fig. 6F and Supplementary Fig. S8). The quantitative analysis of the number of dots per cell confirmed the occurrence of a significant interaction between both APE1 and AUF1 and the D:R hybrid structures.

Altogether, the earlier reported data demonstrated that the APE1–AUF1 interaction is important for the formation of the R-loops, suggesting that APE1 plays a main role in their resolution.

Discussion

In this work, we used an unbiased trapping approach to identify 8-oxo-guanosine-binding proteins; among them, we selected AUF1 as a putative candidate assisting damage removal. Further experiments allowed us to demonstrate that AUF1 stably binds to 8-oxo-guanosine and promotes the endoribonuclease activity of APE1 on it. AUF1, also named hnRNP D, is a ribonucleoprotein playing multiple roles (Moore et al., 2014), and it is especially involved in RNA metabolism. AUF1 principal role is represented by its capability to bind to the ARE sequence present on the 3′-untranslated regions of several mRNAs, thus regulating the stability of different target transcripts (Yoon et al., 2014).

Recent publications from Ishii et al. (2018) and Ishii et al. (2015) demonstrated an intriguing role of AUF1 in recognizing and binding oxidized mRNA (Hayakawa et al., 2010; Ishii and Sekiguchi, 2019); however, the fate of the oxidized mRNA bound by AUF1 still remains an open question (Ishii and Sekiguchi, 2019). We previously observed that APE1 depletion promotes the accumulation of oxidized RNA in human cells (Vascotto et al., 2009) and oxidized miRNAs in cancer cells (Antoniali et al., 2017). Interestingly, we demonstrated that APE1 can interact with the nuclear exosome complex and is involved in CisPt-damaged RNA (Codrich et al., 2022). Moreover, we found that APE1 is released through exosome vesicles by cancer cells on genotoxic treatment (Mangiapane et al., 2021) together with some of its regulated miRNAs (Mangiapane et al., in preparation). Based on what we have found in the present study on 8-oxo-guanosine, it is possible that AUF1 may also promote the APE1 endoribonuclease activity on oxidized RNA. Further studies are necessary to address this issue.

Regarding the mechanism explaining the stimulatory role played by AUF1 in the APE1 endoribonuclease activity, a reasonable hypothesis is that AUF1 may act as a stabilizer of the substrate lesion, allowing the NIR activity of APE1 to efficiently proceed. The presence of denaturing agent-resistant protein-DNA complexes in the endonuclease assays was suggestive of the formation of covalently bound intermediate complexes between AUF1 and 8-oxo-guanosine, in a similar way to what happens in the case of topoisomerases (Cho and Jinks-Robertson, 2018; Ide et al., 2018).

Interestingly, it has been demonstrated that APE1 is able to remove 3′-tyrosyl residues from 3′-recessed and nicked DNAs, suggesting a potential role in processing covalent topoisomerase I-DNA intermediates formed during chromosome relaxation (Wilson, 2003). Remarkably, Top1 was also identified in our unbiased approach centered at identifying 8-oxo-guanosine-binding proteins. Based on the data reported in this study, it is tempting to speculate that, during the reaction initiated by AUF1, a protein-DNA covalent adduct may form, possibly leading to the generation of a proper substrate for APE1 enzymatic activity.

The involvement of BER enzymes in coping with the generation of protein cross-links under oxidative stress conditions has already been suggested (Quiñones et al., 2020). The biological relevance of the AUF1–APE1 interaction was further proved by demonstrating that it is modulated by oxidative stress conditions, and by analyzing the effect of AUF1 depletion in terms of accumulation of abasic sites, formation of double-strand breaks, and generation of D:R hybrids.

Our data show that oxidative stress promotes a reduction of the APE1–AUF1 interaction, which is suggestive for the existence of a dynamic cycle in the stoichiometry of complex formation between these two proteins; this seems coherent with protein enzymatic functions we observed in this work. Moreover, we observed that the depletion of AUF1 caused: (i) increased formation of AP-sites; (ii) the generation of γH2AX-positive foci in parallel with comet-positive cells; and (iii) an increase of R-loop structures, which agrees with a previous publication demonstrating its involvement in the processing of D:R hybrids (Alfano et al., 2019).

These results allow us to *bona fide* include AUF1 in the group of regulatory proteins involved in DNA repair mechanisms. Further studies are necessary to better investigate this hypothesis and to understand to which extent AUF1 is essential to cope with different non-canonical DNA lesions. Additional investigations are also needed to ascertain whether backup mechanisms evolved to compensate for any functional impairment due to APE1 loss of function and/or expression.

A limitation of this study is linked to the impossibility to map the expected accumulation of 8-oxo-guanosine embedded in DNA as a consequence of AUF1 depletion; this is because the rNMP-mapping protocols available so far have been designed to map natural rNMPs embedded in DNA and cannot distinguish a normal rNMP from a modified one (Balachander et al., 2020; Koh et al., 2015a) and references therein. Moreover, it is presently impossible for us to demonstrate whether AUF1 localizes alone and/or in combination with APE1 onto 8-oxo-guanosine embedded in DNA.

Indeed, there are actually no validated experimental strategies available that are able to directly and specifically detect oxidized rNMP (*i.e.,* 8-oxo-guanosine) embedded in cellular DNA as well as discriminating 8-oxo-guanosine from 8-oxo-deoxyguanosine. Some techniques that rely on the use of specific antibodies directed *versus* oxidized guanine are not suitable for their incapacity to specifically discriminate 8-oxo-guanosine from 8-oxo-deoxyguanosine. Future studies are, therefore, needed to fill in all these missteps.

As anticipated earlier, other proteins were eluted by our fishing out approach with an intriguing interest, including PCBP1 and MPG that have drawn our attention. Both proteins are mostly involved in DNA repair and RNA metabolism (Jobert and Nilsen, 2014; Liu et al., 2020; Mohanty

et al., 2021). Indeed, recently it was demonstrated that PCBP1, also called hnRNP E1, is able to bind poly-C rich DNA tracts that are present in several oncogene promoters, as well as telomeres, thus monitoring the genome integrity (Mohanty et al., 2021). Moreover, PCBP1 knock-down cells show an increase in DNA damage and mutations (Mohanty et al., 2021).

In a study by Liu et al. (2020), MS analysis confirmed the presence of abasic sites in RNA molecules, often coupled with R-loops. To discover the proteins able to process the RNA abasic sites, the authors identified MPG as a putative candidate to collaborate with APE1 in the recognition and cleavage of RNA abasic sites in D:R hybrids. Another important player that came out from our analysis and deserved further study is Top1. Interestingly, its possible role in repairing ribonucleotides embedded in DNA was already suggested in a recent work (Promonet et al., 2020).

Considering our data and the earlier mentioned publications, we suggest that AUF1 may represent an actor in the processing of damaged rNMPs embedded in DNA and, besides PCBP1, MPG and Top1, a putative candidate in the processing of damaged RNA. Given the importance of the earlier mentioned proteins in the DNA and RNA repair field, we are planning to deeply explore their role in processing 8-oxo-guanosine in DNA as well as in repairing damaged RNA shortly.

To investigate the APE1 and AUF1 overall influence and association with tumorigenesis, we made additional analyses by following a global approach querying the cancer datasets from The Cancer Genome Atlas (TCGA). Specifically, we analyzed all the TCGA datasets associated with RNA-seq data ($n = 44$) and measured, on a *per sample* basis, the correlation existing between APE1 and AUF1 gene expression, represented by the mRNA median z-scores of every patient (Supplementary Fig. S9A).

Out of 33 datasets, where a significant correlation was obtained, glioblastoma (GBM) and brain lower grade glioma (LGG) were the second and the ninth dataset showing the highest positive correlations ($\rho = 0.46$ and $\rho = 0.37$, respectively). We were particularly interested in these two datasets for several reasons. The involvement of APE1 in neurological diseases and neurodegeneration has already been recognized, principally for its role in processing oxidative damage, which is a distinctive type of damage in neurons (Ströbel et al., 2017; Yang et al., 2020).

Regarding AUF1, its involvement is partially explored so far (Moore et al., 2014). Recent studies have demonstrated its indirect role as a regulator of protein (Abdelmohsen et al., 2012; Liu et al., 2022; Oe et al., 2022; Oe et al., 2021), mRNA (Ishii et al., 2015; White et al., 2017), or miRNA (Min et al., 2017) function and stability, having an important role in neurons. We wondered whether APE1 and AUF1 were also differentially expressed in tumor samples. Thus, we queried the TCGA-GBM ($n = 163$) and TCGA-LGG ($n = 518$) datasets through the GEPIA2 portal, using their matched normal samples as a reference, finding that both genes were significantly up-regulated in tumors (Supplementary Fig. S9B, C; |Log2FC| cutoff: 1; *p*-value cutoff: 0.01).

Finally, given the accumulation of D:R hybrids in neurological disorders (*e.g.,* the Aicardi Goutières syndrome), we believe that APE1 and AUF1, as well their interaction, may be involved in the processing of this damage, especially in neurons. Further studies are needed to explore this hypothesis.

Materials and Methods

Oligonucleotides

All the oligonucleotides were purchased, re-suspended, and annealed as described by Malfatti et al. (2017). The biotinylated complementary strand (5′-Biotin TEG—GTTCAGGCCTAACACTACCGGATCC-3′) was purchased from Metabion (Planegg, Germany), purified with HPLC, and re-suspended with RNase- and DNase-free water at a final concentration of 100 μM. Hundred picomole of the biotinylated oligonucleotide was annealed with an excess (150 pmol) of labeled modified DNA strand in 10 m*M* Tris–HCl pH 7.4 and 10 m*M* $MgCl_2$, heated at 95°C, and cooled down overnight in the dark (Fig. 2A).

Cell culture and transfection, and protein lysates preparation

HEK293T and HeLa cells (ATCC®) were grown in Dulbecco's modified Eagle's medium (EuroClone, Milan, Italy) complemented with 10% fetal bovine serum (FBS), 2 m*M* L-glutamine, 100 U/mL penicillin, and 100 mg/mL streptomycin (EuroClone). After each treatment, cells were collected by trypsinization and centrifuged at 250 *g* for 5 min, and the supernatant was removed. The pellet was washed once with phosphate-buffered saline (PBS) 1 × (Euroclone) and then centrifuged again (250 *g* for 5 min).

For the preparation of NCE, the pellet was re-suspended in a cold hypotonic solution containing 10 m*M* HEPES pH 7.9, 10 m*M* KCl, 0.1 m*M* $MgCl_2$, 0.1 m*M* ethylenediaminetetraacetic acid (EDTA) pH 8.0, which was complemented with 0.1 m*M* DTT, 0.5 m*M* phenylmethylsulfonyl fluoride (PMSF), 1 m*M* protease inhibitor (PI) cocktail (Merck Millipore, Burlington, MA), 1 m*M* NaF, and 1 m*M* Na_3VO_4. After centrifugation at 800 *g* for 10 min, at 4°C, the cytosolic proteins were collected whereas intact nuclei were pelleted. The pellet was washed to discard any contamination from the cytosol; then, it was re-suspended with a cold hypertonic solution 20 m*M* HEPES pH 7.9, 420 m*M* NaCl, 1.5 m*M* $MgCl_2$, 0.1 m*M* EDTA pH 8.0, 5% (w/v) glycerol complemented with 0.1 m*M* DTT, 0.5 m*M* PMSF, 1 m*M* PI, 1 m*M* NaF, and 1 m*M* Na_3VO_4, and finally incubated on ice for 30 min.

At the end of the treatment, the sample was centrifuged at 15,000 *g* for 20 min, at 4°C, and the supernatant containing nuclear proteins (NCE) was collected. For the preparation of whole cell extracts, the cell pellet was resuspended in the lysis buffer containing 50 m*M* Tris-HCl (pH 7.4), 150 m*M* NaCl, 1 m*M* EDTA, 1% w/v Triton X-100 supplemented with 1 m*M* PI, 1 m*M* DTT, 0.5 m*M* PMSF, 1 m*M* NaF, and 1 m*M* Na_3VO_4, for 30 min, at 4°C. After centrifugation at 15,000 *g* for 20 min, at 4°C, the supernatant was collected as a whole cell lysate.

The concentration of each protein sample was determined with the colorimetric Bradford assay (Bio-Rad, Hercules, CA). Twenty-four hours before transient transfection, HeLa cells were seeded on 6-wells (300,000 cells) or on 24-wells (80,000 cells) multiwells. For protein silencing, 100 pmol of siRNA APE1 5′-UACUCCAGUCGUACCAGACCU-3′ (Dharmacon, Lafayette, CO), ON-TARGETplus SMART pool Human HNRNPD (L-004079-00-0020; Dharmacon), or the Scramble control siGENOME non-Targeting siRNA Pool #2 (FE5D0012061420; Dharmacon) were transfected by using the DharmaFECT reagent (Dharmacon).

After 48 h from transfection, cells were collected. For protein overexpression, 2 μg of pFLAG-CMV5.1/Empty, pFLAG-CMV2/AUF1 (kindly provided from Prof. Je-Hyun Yoon), pFRT_TO_DESTFLAGHA [Addgene, Watertown, MA, plasmid # 26361; http://n2t.net/addgene:26361; RRID:Addgene_26361 (Spitzer et al., 2011), kindly provided from Dr. Thomas Tuschl] and pFRT-DestFLAGHA_RNAseH1 [Addgene plasmid # 65783; http://n2t.net/addgene:65783; RRID:Addgene_65783 (Spitzer et al., 2011), kindly provided from Dr. Thomas Tuschl] were transfected by using Lipofectamine 2000 (Invitrogen, Waltham, MA).

Southwestern blot

Briefly, 100 μg of NCE from HEK293T were loaded in a 12% T sodium dodecyl sulfate–polyacrylamide gel electrophoresis (SDS-PAGE) and blotted onto nitrocellulose. The membrane was first incubated with 6 *M* Gdn-HCl freshly dissolved in RNase-free SWB buffer containing 10 m*M* HEPES pH 7.9, 50 m*M* NaCl, 10 m*M* $MgCl_2$, 0.1 μ*M* EDTA, 1 m*M* DTT, 50 μ*M* $ZnSO_4$, and 0.1% (w/v) Tween-20 for 10 min, and then incubated six times with 1:1 Gdn-HCl serial dilutions, for 10 min each, at 4°C, for protein renaturation.

After washing two times with the SWB buffer, the filter was blocked in 5% non-fat dry milk in the SWB buffer for 1 h, at room temperature, and then with the label oligonucleotides (50 pmol) in the presence of 0.25% (w/v) BSA and 10 μg/mL polydIdC, overnight, at 4°C. The day after, the filter was washed with the SWB buffer and acquired with an Odyssey CLx Infrared Imaging system (LI-COR Biosciences GmbH).

Biotin/streptavidin-based capturing approach

Streptavidin-covered Dynabeads (Life Technologies) were placed on a magnet and the supernatant was discarded. First, Dynabeads were washed twice in Solution A (DEPC-treated 0.1 *M* NaOH and 0.05 *M* NaCl) for 2 min, and then twice in Solution B (DEPC-treated 0.1 *M* NaCl). Before the incubation with the sample, Dynabeads were washed once in the EMSA binding buffer containing 8 m*M* HEPES, 10 m*M* KCl, 0.4 m*M* EDTA and 2% (w/v) glycerol.

The incubation among NCE and Biot-oligonucleotides was carried on ice for 1.5 h, and it was preceded by NCE preclearing on RNase-free Dynabeads for 10 min. Then, recovered DNA-protein complexes were incubated with the Dynabeads for 10 min, at room temperature. The Dynabeads were washed four times with the EMSA binding buffer. Elution was carried by different NaCl concentrations for 10 min, on a rocker. Lastly, the Dynabeads were also resuspended with Laemmli buffer 1×.

All the NaCl-eluted samples were precipitated by adding 5 vol of cold acetone, mixed for inversion, and incubated overnight, at −20°C. The day after, samples were centrifuged at 15,000 *g* for 15 min, at 4°C, the acetone was discarded, and the pellet was washed with cold 20% (v/v) methanol. After the centrifugation, the pellet was dried on air, and it was resuspended in Laemmli buffer 1×for further protein gel electrophoretic analysis.

Proteomic experiments

The pellets from each sample were also dissolved in 100 μL of 100 m*M* triethylammonium bicarbonate (TEAB), reduced with 5 μL of 200 m*M* tris(2-carboxyethylphosphine) and incubated for 60 min, at 55°C, and finally alkylated by adding 5 μL of 375 m*M* iodoacetamide, followed by incubation for 30 min in the dark, at room temperature. Reduced and alkylated proteins were then precipitated overnight by addition of 6 vol of cold acetone. After precipitation, proteins were pelleted by centrifugation at 8000 *g* for 10 min, at 4°C, and finally air dried. Each pellet was digested with freshly prepared trypsin (2.5 μg) in 100 m*M* TEAB, at 37°C, overnight.

The resulting peptide samples were subjected to a desalting/concentration step on μZipTipC18 (Millipore Corp., Bedford, MA), vacuum-dried, and finally reconstituted in 0.1% formic acid for subsequent mass spectrometry analysis. Samples were analyzed on a nanoLC-ESI-Q-Orbitrap-MS/MS platform consisting of an UltiMate 3000 HPLC RSLC nano system-Dionex coupled with a Q-ExactivePlus mass spectrometer through a Nanoflex ion source (Thermo Fisher Scientific, Waltham, MA). Peptides were loaded on an Acclaim PepMap™ RSLC C18 column (150 mm × 75 μm ID, 2 μm particles, 100 Å pore size; Thermo Fisher Scientific), and they were eluted with a gradient of solvent B (19.92/80/0.08 v/v/v water/acetonitrile/formic acid) in solvent A (99.9/0.1 v/v water/formic acid), at a flow rate of 300 nL/min.

The gradient of solvent B started at 3%, increased to 60% over 125 min, raised to 95% over 1 min, remained at 95% for 8 min, and finally returned to 3% in 1 min, with a column equilibrating step of 20 min before the subsequent chromatographic run. The mass spectrometer operated in data-dependent mode, using a full scan (*m/z* range 375–1500), nominal resolution of 70,000 automatic gain control target of 3,000,000, a maximum ion target of 50 ms, followed by MS/MS scans of the 15 most abundant ions.

The MS/MS spectra were acquired using a normalized collision energy of 32%, an automatic gain control target of 100,000, a maximum ion target of 120 ms, and a resolution of 17,500. A dynamic exclusion value of 30 s was also used. Two technical replicates were analyzed for each sample.

Raw mass data files per sample were merged for protein identification into the Proteome Discoverer v2.2 software (Thermo Scientific), enabling the database search by the Mascot algorithm v2.4.2 (Matrix Science, United Kingdom) using the following criteria: UniProtKB protein database (*Homo sapiens* as taxonomy October 2018) including the most common protein contaminants, carbamidomethylation of Cys as fixed modification, oxidation of Met, deamidation of Asn and Gln, pyroglutamate formation of Gln as variable modifications. The peptide mass tolerance was set to ±10 ppm and fragment mass tolerance to ±0.05 Da. The proteolytic enzyme and maximum number of missed cleavages were set to trypsin and 2, respectively. Protein candidates with a Mascot score ≥25 were considered confidently identified. The results were filtered to 1% false discovery rate.

Proteomic data have been deposited to the ProteomeXchange Consortium *via* the PRIDE (Perez-Riverol et al., 2019) partner repository with dataset identifier PXD027252.

The interactomes of the three oligonucleotides ds_rG:dC_Biot ($n = 1474$), ds_rF:dC_Biot ($n = 1202$) and ds_r8oxoG:dC_Biot ($n = 1458$), defined merging the proteins identified at two different NaCl concentrations (300 and 400 m*M*), were compared to each other. Functional

enrichment analysis was performed on the ds_rF:dC_Biot and ds_r8oxoG:dC_Biot interactomes using the Cytoscape plugin ClueGO to identify enriched terms (Bindea et al., 2009; Shannon et al., 2003). The following functional databases were queried: CLINVAR_Human-diseases (December 14, 2018), WikiPathways (December 14, 2018), KEGG (December 14, 2018), KEGG-HUMAN-DISEASE (December 14, 2018), REACTOME_Reactions (December 12, 2018), REACTOME_Pathways (December 14, 2018), GO_ImmuneSystemProcess (December 14, 2018), GO_BiologicalProcess (December 14, 2018), and CORUM_CORUM-FunCat-MIPS (December 14, 2018).

A right-sided hypergeometric test (corrected using the Benjamini-Hochberg method to control the false discovery rate, adjusted $p \leq 0.05$) was used to determine the probability that each functional term was assigned to the gene sets due to chance alone. Default parameters were used except for: Min#Genes = 80, Min Percentage = 10.0%, Cluster to be Significant = 80.0%, Min GO Level = 7, Max GO Level = 15.

We extracted the ''rna_seq_v2_mrna'' gene expression levels of APE1 and AUF1 in 44 TCGA datasets and calculated the pairwise correlations using the R/Bioconductor cgdsr package for querying the Cancer Genomics Data Server (CGDS), hosted by the Computational Biology Center at Memorial-Sloan-Kettering Cancer Center (MSKCC) (Jacobsen and Augustin, 2019). The statistically significant correlations were summarized as bar plots.

We evaluated the APE1 and AUF1 gene expression levels in the TCGA-GBM ($n = 163$) and TCGA-LGG ($n = 518$) cancer datasets and compared them with the TCGA-GTEx matched normal samples ($n = 207$). Data were obtained from the GEPIA2 web server (http://gepia2.cancer-pku.cn/#analysis, last accessed October 2021) and summarized as boxplots; |Log2FC| Cutoff: 1; p-value cutoff: 0.01.

Immunoblotting analysis

For immunoblotting analyses, 30 μg of nuclear or whole cell lysates were resolved on 12% T SDS–PAGE and transferred onto nitrocellulose membranes (Schleicher & Schuell Bioscience, Dassel, Germany). The following antibodies were used in this study: AUF1 (1:1000, sc-166577; Santa Cruz Biotechnology, Dallas, TX), APE1 (1:2000, NB 100-116; Novus Biological, Minneapolis, MN), GST (1:2000, ab19256; Abcam, Cambridge, United Kingdom), PrxSO3 (1:2000, ab16830; Abcam), H3 (1:1000, A300-823A-M; Bethyl Laboratories, Waltham, MA), actin (1:3000, A 2066; Merck Millipore), and tubulin (1:3000, T 0198; Merck Millipore).

The antibodies were diluted in TBS with 0.1% (v/v) Tween-20 and incubated overnight, at 4°C, or for 2 h, at room temperature. Revert™ 700 Total Protein Stain was used for Western Blot Normalization (926-11011; LI-COR Biosciences GmbH). Original uncropped images of Western blots used in this study can be found in Supplementary Figures S10–S13.

EMSA and enzymatic assays

The EMSA and enzymatic assays were performed as described by Malfatti et al. (2017). For EMSA, the reactions were prepared by incubating rAUF1, as indicated, with 250 fmol of the substrate (0.025 μM) in EMSA binding buffer, for 2 h, at 4°C. When co-incubated with rAPE1, the reactions were marginally modified incubating rAUF1 for 1.5 h, at 4°C, and then adding rAPE1, as indicated, for 30 min, at 4°C. The mixtures were loaded on a native gel 8% T polyacrylamide, and then run at 4°C at 150 V, for 1 h, and then increasing at 250 V, for 3 h, in 0.5 × TAE buffer. The gels were scanned, and band intensities were quantified using the Image Studio software (Odyssey CLx; LI-COR Biosciences GmbH).

To measure the enzymatic activity of recombinant proteins, the oligonucleotide substrates (25 nM) were incubated with different amounts of proteins for different timing points, as indicated in each figure. Reactions were carried on in a buffer containing 10 mM TrisHCl pH 7.4, 1 mM $MgCl_2$, 25 mM KCl. When the proteinase K treatment was performed, 1 μg of the protease was added at the end of the reaction, and the mixture was incubated for 30 min, at 50°C. At the end of all reactions, samples were blocked with a stop solution, containing 99.5% (v/v) formamide (Merck Millipore) supplemented with 10 × Orange Loading Dye (LI-COR Biosciences GmbH) and heated at 95°C, for 5 min.

All samples were then loaded onto a 7 M urea denaturing 20% T polyacrylamide gel in TBE buffer pH 8.0, and then run at 4°C, at 300 V, for 1 h. Afterward, the gel was visualized with an Odyssey CLx Infrared Imaging system (LI-COR Biosciences GmbH). The signals of the non-incised substrate (S) and the incision product (P) bands were quantified using Image Studio software (LI-COR Biosciences GmbH). Statistical analyses were performed by using the Student's t-test, Mann–Whitney, or one-ANOVA, as needed. $p = 0.05$ or lesser was considered as statistically significant.

UV-crosslinking analysis

UV-crosslinking analyses were performed as described by Burra et al. (2019). rAUF1, which was present at different concentrations (as indicated), was incubated with 250 fmol of oligonucleotides in EMSA binding buffer, for 1.5 h, at 4°C. Then, the mixtures were UV-crosslinked using a Vilber Lourmat UV-crosslinker BLX-254 at 0.2 J/cm^2, denaturized in Laemmli buffer 4 ×, boiled at 95°C, for 5 min, and run onto 8% T SDS-PAGE gel.

Proximity ligation assay (PLA) and γH2AX foci levels quantification

PLA and γH2AX immunofluorescence analysis was performed as described by Codrich et al. (2019). For γH2AX immunofluorescence analysis, 80,000 cells were seeded on glass slides. Forty-eight hours after the indicated transfection, the cells were fixed with 4% (w/v) paraformaldehyde for 20 min, at room temperature, permeabilized with 0.25% Triton X-100 in PBS 1 ×, for 5 min, at room temperature, and then incubated with 10% FBS, at room temperature, overnight.

The day after, the cells were incubated with 1:500 anti-phospho-Histone H2AX (Ser139), clone JBW301 antibody (05-636; Merck Millipore) for 2 h, at 37°C, and then with 1:100 anti-mouse Alexa Fluor® 488 secondary antibody (Jackson ImmunoResearch, West Grove, PA) for 1.5 h, at room temperature. DNA was stained with 14.3 mM DAPI (Thermo Fisher Scientific) for 5 min, at room temperature. Glass slides were mounted with DABCO mounting and

visualized using a laser scanning confocal microscope (LEICA TCS SP8; Leica Microsystems, Wetzlar, Germany).

For PLA assay, 80,000 cells were seeded on glass slides. Forty-eight hours after the indicated transfection, cells were fixed with 4% (w/v) paraformaldehyde for 20 min, at room temperature, and then permeabilized with 0.25% (w/v) Triton X-100 in PBS 1×, for 5 min, at room temperature. After blocking with 10% FBS for 30 min, at room temperature, the cells were incubated with the following primary antibodies: 1:500 anti-AUF1 (sc-166577; Santa Cruz) or 1:400 anti-FLAG (A8592; Merck) for 2 h, at 37°C, and 1:100 anti-APE1 (NB 100-101; Novus Biological), at room temperature, overnight.

When 1:500 anti-DNA:RNA hybrid [S9.6], clone D5H6 antibody (mab0105-P; Covalab, Bron, France) was used, the cells were fixed with 10% v/v methanol, for 10 min, at −20°C, permeabilized with 0.1% (w/v) Triton X-100 in PBS 1×, for 5 min, at room temperature, and finally blocked with 5% (w/v) BSA for 30 min, at room temperature.

The Proximity ligation assay (PLA) was conducted according to the manufacturer's instructions, first incubating with the PLA probes for 1 h, at 37°C, then with the ligase for 30 min, at 37°C, and finally with the polymerase for 100 min, at 37°C. DNA was stained with 14.3 m*M* DAPI (Thermo Fisher Scientific) for 5 min, at room temperature. The glass slides were mounted with DABCO mounting and visualized using a laser scanning confocal microscope (LEICA TCS SP8; Leica Microsystems).

GST-pulldown analysis

Hundred picomole of rGST, rGST-APE1^{WT} and rGST-APE1$^{N\Delta 33}$ proteins were incubated with 100 pmol of rAUF1 in the EMSA binding buffer complemented with freshly 1 m*M* DTT and 0.5 m*M* PMSF, for 50 min, at 37°C, in a final volume of 100 μL. After carefully washing three times with the EMSA binding buffer complemented with freshly 1 m*M* DTT and 0.5 m*M* PMSF, and centrifuging at 8000 *g*, for 1 min at 4°C, 10 μL of Glutathione Sepharose® 4B (GE Healthcare, Chicago, IL) were incubated with the protein mixture, for 30 min, at 4°C, on a rocker.

Before elution, 30 μL of the resin-protein complexes were conserved. After centrifugation, the supernatant was conserved as ''Flow through sample,'' whereas the pelleted resin-protein complexes were washed for 10 times with the EMSA binding buffer complemented with freshly 1 m*M* DTT, 0.5 m*M* PMSF, and 0.1% (w/v) NP40. The elution was performed by adding 10 m*M* GSH to the EMSA binding buffer complemented with freshly 1 m*M* DTT and 0.5 m*M* PMSF, for 30 min, at 4°C, on a rocker.

Metabolic activity and colony formation assay

Metabolic activity of cells was measured through the RealTime-Glo™ MT Cell Viability Assay (Promega, Madison, WI), as already reported by Codrich et al. (2019). For colony formation assays, 1.50×10^2 HeLa cells were seeded onto six-well plates and were silenced the day after. Twenty-four hours later, the medium was replaced, and the cells were allowed to form visible colonies in fresh medium. After 10 days, cell colonies were washed with PBS 1×, stained with 10% (w/v) of crystal violet diluted in 70% (v/v) ethanol, and washed again with distilled H_2O. Six-wells plates were scanned by using the Image Studio software (Odyssey CLx; LI-COR Biosciences GmbH), and the number of colonies for each condition was determined.

Comet assay and AP sites measurements

Forty thousand cells were plated on 24-well plates and the day after cells were silenced. After 48 h, cells were collected and mixed with low melting point agarose, at 37°C, and the mixture was applied to an agarose pre-coated glass coverslip to form a thin layer. Cold lysis buffer was added to lyse cells at 4°C. After 1 h, the glass coverslip was moved into the alkaline electrophoresis buffer, for 30 min, to unwind DNA.

Electrophoresis was carried out at 25 V and 300 mA, for 30 min. The glass coverslip was washed with the neutralizing buffer for three times and stained by SYBER Gold 1×(Thermo Fisher Scientific) for 30 min, in the dark. Comets were recorded by the laser scanning confocal microscope (LEICA TCS SP2; Leica Microsystems). The tail moment was analyzed for 100 cells at random by the OpenComet software.

For the AP sites measurements, the genomic DNA was extracted from 48 h-silenced HeLa cells using QIAamp DNA Mini Kit (Qiagen, Hilden, Germany), and the corresponding concentration and purity were determined by using the Qubit 4 Fluorometer (Thermo Fisher Scientific). AP site measurements were measured through the DNA Damage Quantification Kit -AP Site Counting- (Dojindo Molecular Technologies, Kumamoto, Japan) according to the manufacturer's instructions.

Northwestern and DRIP analysis

For northwestern analysis, the genomic DNA was purified by using the QIAamp DNA Mini Kit (Qiagen); 0.5 μg of purified genomic DNA was blotted onto a nitrocellulose membrane by using a vacuum slot-blot apparatus (GE Healthcare) following the manufacturer's instructions. Then, the membrane (GE Healthcare) was UV-crosslinked by using a Vilber Lourmat UV-crosslinker BLX-254 at 0.12 J/cm^2. After blocking reaction with 5% (w/v) BSA in TBS containing 0.1% (w/v) Tween 20, for 1 h, the membrane was incubated with 1:1000 D:R hybrids antibody (clone S9.6, mab0105-P; Covalab) and 1:1000 ssDNA (MAB3034; Millipore) at 4°C, overnight.

The membrane was scanned, and band intensities were quantified using the Image Studio software (Odyssey CLx; LI-COR Biosciences GmbH). DRIP was performed as described in Cristini et al. (2018). The cells were lysed in the lysis buffer containing 85 m*M* KCl, 5 m*M* PIPES (pH 8.0), and 0.5% (w/v) NP-40. The pelleted nuclei were resuspended in RSB buffer containing 10 m*M* Tris-HCl pH 7.5, 200 m*M* NaCl, 2.5 m*M* $MgCl_2$ complemented with 0.2% (w/v) sodium deoxycholate, 0.1% (w/v) SDS, 0.05% (w/v) sodium lauroyl sarcosinate (Na sarcosyl), and 0.5% (w/v) Triton X-100.

By using a Diagenode Bioruptor, we sonicated the samples until the DNA fragments size from DNA:RNA hybrid IP samples was around 500 bp. Control and RNase A (R5125; Merck Millipore)-treated samples were subjected to immunoprecipitation by using S9.6 conjugated magnetic protein A Dynabeads®. The elution was performed by Laemmli buffer 1×, and samples were boiled at 95°C. The input and eluted samples were separated on a 12%–10% T bi-phasic SDS-PAGE gel and blotted on a nitrocellulose membrane.

Raw data storage

Electronic laboratory notebook was not used but all raw data are stored in Synology NAS http://labgt.synology.me:5000/

Acknowledgments

The authors thank Dr. Michael Musheev for fruitful suggestions.

Proteomic Data Depository

Proteomic data have been deposited to the ProteomeXchange Consortium *via* the PRIDE partner repository with dataset identifier PXD027252.

Authors' Contributions

G.T. designed and conceived the study and supervised the experiments; M.C.M. performed all the experiments, analyzed the data, and critically contributed to the interpretation of the results; M.C. contributed to the acquisition of images at the confocal microscope and contributed to D:R hybrid experiments; E.D. performed the bioinformatic analysis; C.D.A. and A.S. performed MS analysis and analyzed the data; M.C.M. and G.T. mainly wrote the manuscript. M.C., E.D., C.D.A., F.S., and A.S., provided critical comments and suggestions and contributed to the interpretation of the results. All authors critically read and approved the final version of the manuscript.

Author Disclosure Statement

No competing financial interests exist.

Funding Information

This work was supported by funding from the NIH, United States R01 ES026243 (Francesca Storici), the Howard Hughes Medical Institute Faculty Scholar (grant 55108574 to Francesca Storici) and by AIRC under IG 2017—ID. 19862 (Gianluca Tell).

Supplementary Material

Supplementary Figure S1
Supplementary Figure S2
Supplementary Figure S3
Supplementary Figure S4
Supplementary Figure S5
Supplementary Figure S6
Supplementary Figure S7
Supplementary Figure S8
Supplementary Figure S9
Supplementary Figure S10
Supplementary Figure S11
Supplementary Figure S12
Supplementary Figure S13
Supplementary Table S1

References

Abdelmohsen K, Tominaga-Yamanaka K, Srikantan S, et al. RNA-binding protein AUF1 represses dicer expression. Nucleic Acids Res 2012;40(22):11531–11544; doi: 10.1093/nar/gks930

Agarwal P, Miller KM. The nucleosome: Orchestrating DNA damage signaling and repair within chromatin. Biochem Cell Biol 2016;94(5):381–395; doi: 10.1139/bcb-2016-0017

Alam MS. Proximity ligation assay (PLA). Curr Protoc Immunol 2018;123(1):e58; doi: 10.1002/cpim.58

Alfano L, Caporaso A, Altieri A, et al. Depletion of the RNA binding protein HNRNPD impairs homologous recombination by inhibiting DNA-end resection and inducing R-loop accumulation. Nucleic Acids Res 2019;47(8):4068–4085; doi: 10.1093/nar/gkz076

Amouroux R, Campalans A, Epe B, et al. Oxidative stress triggers the preferential assembly of base excision repair complexes on open chromatin regions. Nucleic Acids Res 2010;38(9):2878–2890; doi: 10.1093/nar/gkp1247

Antoniali G, Serra F, Lirussi L, et al. Mammalian APE1 controls miRNA processing and its interactome is linked to cancer RNA metabolism. Nat Commun 2017;8(1):797; doi: 10.1038/s41467-017-00842-8

Balachander S, Gombolay AL, Yang T, et al. Ribonucleotide incorporation in yeast genomic DNA shows preference for cytosine and guanosine preceded by deoxyadenosine. Nat Commun 2020;11(1):2447; doi: 10.1038/s41467-020-16152-5

Barnes T, Kim W-CC, Mantha AK, et al. Identification of apurinic/apyrimidinic endonuclease 1 (APE1) as the endoribonuclease that cleaves c-Myc mRNA. Nucleic Acids Res 2009;37(12):3946–3958; doi: 10.1093/nar/gkp275

Batra VK, Beard WA, Pedersen LC, et al. Structures of DNA polymerase mispaired DNA termini transitioning to pre-catalytic complexes support an induced-fit fidelity mechanism. Structure 2016;24(11):1863–1875; doi: 10.1016/j.str.2016.08.006

Bindea G, Mlecnik B, Hackl H, et al. ClueGO: A cytoscape plug-in to decipher functionally grouped gene ontology and pathway annotation networks. Bioinformatics 2009;25(8): 1091–1093; doi: 10.1093/bioinformatics/btp101

Brown JA, Suo Z. Unlocking the sugar ''Steric Gate'' of DNA polymerases. Biochemistry 2011;50(7):1135–1142; doi: 10.1021/bi101915z

Burra S, Marasco D, Malfatti MC, et al. Human AP-endonuclease (Ape1) activity on telomeric G4 structures is modulated by acetylatable lysine residues in the N-terminal sequence. DNA Repair (Amst) 2019;73:129–143; doi: 10.1016/j.dnarep.2018.11.010

Cai Y, Geacintov NE, Broyde S. Ribonucleotides as nucleotide excision repair substrates. DNA Repair (Amst) 2014;13(1): 55–60; doi: 10.1016/j.dnarep.2013.10.010

Cerritelli SM, Iranzo J, Sharma S, et al. High density of unrepaired genomic ribonucleotides leads to topoisomerase 1-mediated severe growth defects in absence of ribonucleotide reductase. Nucleic Acids Res 2020;48(8):4274–4297; doi: 10.1093/nar/gkaa103

Chiu H-C, Koh KD, Evich M, et al. RNA intrusions change DNA elastic properties and structure. Nanoscale 2014;6(17): 10009; doi: 10.1039/C4NR01794C

Cho JE, Jinks-Robertson S. Topoisomerase I and genome stability: The good and the bad. Methods Mol Biol 2018;1703: 21–45; doi: 10.1007/978-1-4939-7459-7_2

Cilli P, Minoprio A, Bossa C, et al. Formation and repair of mismatches containing ribonucleotides and oxidized bases at repeated DNA sequences. J Biol Chem 2015;290(43):26259–26269; doi: 10.1074/jbc.M115.679209

Clausen AR, Lujan SA, Burkholder AB, et al. Tracking replication enzymology in vivo by genome-wide mapping of ribonucleotide incorporation. Nat Struct Mol Biol 2015;22(3): 185–191; doi: 10.1038/nsmb.2957

Codrich M, Comelli M, Malfatti MC, et al. Inhibition of APE1-endonuclease activity affects cell metabolism in colon cancer cells via a P53-dependent pathway. DNA Repair (Amst) 2019;82:102675; doi: 10.1016/j.dnarep.2019.102675

Codrich M, Degrassi M, Malfatti MC, et al. APE1 interacts with the nuclear exosome complex protein MTR4 and is involved in cisplatin- and 5-fluorouracil-induced RNA damage response. FEBS J 2022. [Epub ahead of print]; doi: 10.1111/febs.16671

Cristini A, Groh M, Kristiansen MS, et al. RNA/DNA hybrid interactome identifies DXH9 as a molecular player in transcriptional termination and R-loop-associated DNA damage. Cell Rep 2018;23(6):1891–1905; doi: 10.1016/j.celrep.2018.04.025

Daviet S, Couvé-Privat S, Gros L, et al. Major oxidative products of cytosine are substrates for the nucleotide incision repair pathway. DNA Repair (Amst) 2007;6(1):8–18; doi: 10.1016/j.dnarep.2006.08.001

Fantini D, Vascotto C, Marasco D, et al. Critical lysine residues within the overlooked N-terminal domain of human APE1 regulate its biological functions. Nucleic Acids Res 2010;38(22):8239–8256; doi: 10.1093/nar/gkq691

Ghodke PP, Guengerich FP, Guengerich PF. Impact of 1,N6-ethenoadenosine, a damaged ribonucleotide in DNA, on translesion synthesis and repair. J Biol Chem 2020;295(18):6092–6107; doi: 10.1074/jbc.ra120.012829

Hayakawa H, Fujikane A, Ito R, et al. Human proteins that specifically bind to 8-oxoguanine-containing RNA and their responses to oxidative stress. Biochem Biophys Res Commun 2010;403(2):220–224; doi: 10.1016/j.bbrc.2010.11.011

He H, Chen Q, Georgiadis MM. High-Resolution crystal structures reveal plasticity in the metal binding site of apurinic/apyrimidinic endonuclease i. Biochemistry 2014;53(41):6520–6529; doi: 10.1021/BI500676P

Ide H, Nakano T, Salem AMH, et al. DNA-protein cross-links: Formidable challenges to maintaining genome integrity. DNA Repair (Amst) 2018;71:190–197; doi: 10.1016/J.DNAREP.2018.08.024

Ishchenko AA, Deprez E, Maksimenko A, et al. Uncoupling of the base excision and nucleotide incision repair pathways reveals their respective biological roles. Proc Natl Acad Sci U S A 2006;103(8):2564–2569; doi: 10.1073/pnas.0508582103

Ishii T, Hayakawa H, Igawa T, et al. Specific binding of PCBP1 to heavily oxidized RNA to induce cell death. Proc Natl Acad Sci U S A 2018;115(26):6715–6720; doi: 10.1073/pnas.1806912115

Ishii T, Hayakawa H, Sekiguchi T, et al. Role of Auf1 in elimination of oxidatively damaged messenger RNA in human cells. Free Radic Biol Med 2015;79:109–116; doi: 10.1016/j.freeradbiomed.2014.11.018

Ishii T, Sekiguchi M. Two ways of escaping from oxidative RNA damage: Selective degradation and cell death. DNA Repair (Amst) 2019;81:102666; doi: 10.1016/j.dnarep.2019.102666

Jackson SP, Bartek J. The DNA-damage response in human biology and disease. Nature 2009;461(7267):1071–1078; doi: 10.1038/nature08467

Jacobsen A, Augustin L. Anders Jacobsen and CBioPortal Questions (2018). Cgdsr: R-Based API for Accessing the MSKCC Cancer Genomics Data Server (CGDS). R Package Version 1.2.10; 2019.

Jinks-Robertson S, Klein HL. Ribonucleotides in DNA: Hidden in plain sight. Nat Struct Mol Biol 2015;22(3):176–178; doi: 10.1038/nsmb.2981

Jobert L, Nilsen H. Regulatory mechanisms of RNA function: Emerging roles of DNA repair enzymes. Cell Mol Life Sci 2014;71(13):2451–2465; doi: 10.1007/s00018-014-1562-y

Kellner V, Luke B. Molecular and physiological consequences of faulty eukaryotic ribonucleotide excision repair. EMBO J 2020;39(3):e102309; doi: 10.15252/embj.2019102309.

Koh KD, Balachander S, Hesselberth JR, et al. Ribose-Seq: Global mapping of ribonucleotides embedded in genomic DNA. Nat Methods 2015a;12(3):251–257; doi: 10.1038/nmeth.3259

Koh KD, Chiu HC, Riedo E, et al. Measuring the elasticity of ribonucleotide(s)-containing DNA molecules using AFM. Methods Mol Biol 2015b;1297:43–57; doi: 10.1007/978-1-4939-2562-9_3

Krokan HE, Bjørås M. Base excision repair. Cold Spring Harb Perspect Biol 2013;5(4):1–22; doi: 10.1101/cshperspect.a012583

Li F, Wang Q, Seol JH, et al. Apn2 resolves blocked 3′ ends and suppresses Top1-induced mutagenesis at genomic RNMP sites. Nat Struct Mol Biol 2019;26(3):155–163; doi: 10.1038/s41594-019-0186-1

Liu H, Zheng W, Song Z. CircDlgap4 alleviates cerebral ischaemic injury by binding to AUF1 to suppress oxidative stress and neuroinflammation. Mol Neurobiol 2022;59(5):3218–3232; doi: 10.1007/S12035-022-02796-5

Liu Y, Rodriguez Y, Ross RL, et al. RNA abasic sites in yeast and human cells. Proc Natl Acad Sci U S A 2020;117(34):20689–20695; doi: 10.1073/pnas.2011511117

Lockhart A, Pires VB, Bento F, et al. RNase H1 and H2 are differentially regulated to process RNA-DNA hybrids. Cell Rep 2019;29(9):2890–2900.e5.

Mah L-J, El-Osta A, Karagiannis TC. γH2AX: A sensitive molecular marker of DNA damage and repair. Leukemia 2010;24(4):679–686; doi: 10.1038/leu.2010.6

Malfatti MC, Balachander S, Antoniali G, et al. Abasic and oxidized ribonucleotides embedded in DNA are processed by human APE1 and Not by RNase H2. Nucleic Acids Res 2017;45(19):11193–11212; doi: 10.1093/nar/gkx723

Malfatti MC, Henneke G, Balachander S, et al. Unlike the *Escherichia coli* counterpart, archaeal RNase HII cannot process ribose monophosphate abasic sites and oxidized ribonucleotides embedded in DNA. J Biol Chem 2019;294(35):13061–13072; doi: 10.1074/jbc.ra119.009493

Mangiapane G, Parolini I, Conte K, et al. Enzymatically active apurinic/apyrimidinic endodeoxyribonuclease 1 is released by mammalian cells through exosomes. J Biol Chem 2021;296:100569; doi: 10.1016/j.jbc.2021.100569

McElhinny SAN, Kumar D, Clark AB, et al. Genome instability due to ribonucleotide incorporation into DNA. Nat Chem Biol 2010;6(10):774–781; doi: 10.1038/nchembio.424

Meroni A, Mentegari E, Crespan E, et al. The incorporation of ribonucleotides induces structural and conformational changes in DNA. Biophys J 2017;113(7):1373–1382; doi: 10.1016/j.bpj.2017.07.013

Min KW, Jo MH, Shin S, et al. AUF1 facilitates microRNA-mediated gene silencing. Nucleic Acids Res 2017;45(10):6064–6073; doi: 10.1093/nar/gkx149

Mohanty BK, Karam JAQ, Howley B V., et al. Heterogeneous nuclear ribonucleoprotein E1 binds polycytosine DNA and monitors genome integrity. Life Sci Alliance 2021;4(9):e202000995; doi: 10.26508/LSA.202000995

Moore AE, Chenette DM, Larkin LC, et al. Physiological networks and disease functions of RNA-binding protein AUF1. Wiley Interdiscip Rev RNA 2014;5(4):549–564; doi: 10.1002/wrna.1230

Nakamura J, Walker VE, Upton PB, et al. Highly sensitive apurinic/apyrimidinic site assay can detect spontaneous and chemically induced depurination under physiological conditions. Cancer Res 1998;58(2):222–225.

Nick McElhinny SA, Watts BE, Kumar D, et al. Abundant ribonucleotide incorporation into DNA by yeast replicative polymerases. Proc Natl Acad Sci U S A 2010;107(11):4949–4954; doi: 10.1073/pnas.0914857107

Oe S, Hayashi S, Tanaka S, et al. Cpeb1 expression is post-transcriptionally regulated by AUF1, CPEB1, and microRNAs. FEBS Open Bio 2022;12(1):82–94; doi: 10.1002/2211-5463.13286

Oe S, Koike T, Hirahara Y, et al. AUF1, an mRNA decay factor, has a discordant role in Cpeb1 expression. Biochem Biophys Res Commun 2021;534:491–497; doi: 10.1016/j.bbrc.2020.11.054

Perez-Riverol Y, Csordas A, Bai J, et al. The PRIDE database and related tools and resources in 2019: Improving support for quantification data. Nucleic Acids Res 2019;47(D1):D442–D450; doi: 10.1093/nar/gky1106

Poletto M, Vascotto C, Scognamiglio PL, et al. Role of the unstructured N-terminal domain of the HAPE1 (human apurinic/apyrimidinic endonuclease 1) in the modulation of its interaction with nucleic acids and NPM1 (nucleophosmin). Biochem J 2013;452(3):545–557; doi: 10.1042/bj20121277

Potenski CJ, Klein HL. How the misincorporation of ribonucleotides into genomic DNA can be both harmful and helpful to cells. Nucleic Acids Res 2014;42(16):10226–10234; doi: 10.1093/nar/gku773

Promonet A, Padioleau I, Liu Y, et al. Topoisomerase 1 prevents replication stress at R-loop-enriched transcription termination sites. Nat Commun 2020;11(1):3940; doi: 10.1038/s41467-020-17858-2

Quiñones JL, Thapar U, Wilson SH, et al. Oxidative DNA-protein crosslinks formed in mammalian cells by abasic site lyases involved in DNA repair. DNA Repair (Amst) 2020;87:102773; doi: 10.1016/J.DNAREP.2019.102773

Ramirez P, Crouch RJ, Cheung VG, et al. R-loop analysis by dot-blot. J Vis Exp 2021;2021(167):1–14; doi: 10.3791/62069

Randerath K, Reddy R, Danna TF, et al. Formation of ribonucleotides in DNA modified by oxidative damage *in vitro* and *in vivo*. Characterization by 32P-postlabeling. Mutat Res 1992;275(3–6):355–366.

Shannon P, Markiel A, Ozier O, et al. Cytoscape: A software environment for integrated models of biomolecular interaction networks. Genome Res 2003;13(11):2498–2504; doi: 10.1101/gr.1239303

Sidali A, Teotia V, Solaiman NS, et al. AU-rich element RNA binding proteins: At the crossroads of post-transcriptional regulation and genome integrity. Int J Mol Sci 2021;23(1):96; doi: 10.3390/ijms23010096

Sies H. Hydrogen peroxide as a central redox signaling molecule in physiological oxidative stress: Oxidative eustress. Redox Biol 2017;11:613–619; doi: 10.1016/J.REDOX.2016.12.035

Smith MR, Alnajjar KS, Hoitsma NM, et al. Molecular and structural characterization of oxidized ribonucleotide insertion into DNA by human DNA polymerase β. J Biol Chem 2020;295(6):1613–1622; doi: 10.1074/jbc.RA119.011569

Sparks JL, Chon H, Cerritelli SM, et al. RNase H2-initiated ribonucleotide excision repair. Mol Cell 2012;47(6):980–986; doi: 10.1016/j.molcel.2012.06.035

Spitzer JI, Ugras S, Runge S, et al. MRNA and protein levels of FUS, EWSR1, and TAF15 are upregulated in liposarcoma. Genes Chromosomes Cancer 2011;50(5):338–347; doi: 10.1002/GCC.20858

Ströbel T, Madlener S, Tuna S, et al. Ape1 guides DNA repair pathway choice that is associated with drug tolerance in glioblastoma. Sci Rep 2017;7(1):9674; doi: 10.1038/S41598-017-10013-W

Vaisman A, McDonald JP, Huston D, et al. Removal of misincorporated ribonucleotides from prokaryotic genomes: An unexpected role for nucleotide excision repair. PLoS Genet 2013;9(11):e1003878; doi: 10.1371/journal.pgen.1003878

Vascotto C, Fantini D, Romanello M, et al. APE1/Ref-1 interacts with NPM1 within nucleoli and plays a role in the RRNA quality control process. Mol Cell Biol 2009;29(7):1834–1854; doi: 10.1128/MCB.01337-08

White EJF, Matsangos AE, Wilson GM. AUF1 regulation of coding and noncoding RNA. Wiley Interdiscip Rev RNA 2017;8(2):10.1002/wrna.1393; doi: 10.1002/wrna.1393

Williams JS, Clausen AR, Nick McElhinny SA, et al. Proofreading of ribonucleotides inserted into DNA by yeast DNA polymerase ε. DNA Repair (Amst) 2012;11(8):649–656; doi: 10.1016/j.dnarep.2012.05.004

Williams JS, Kunkel TA. Studying topoisomerase 1-mediated damage at genomic ribonucleotides. Methods Mol Biol 2018;1703;241–257; doi: 10.1007/978-1-4939-7459-7_17

Wilson DM. Properties of and substrate determinants for the exonuclease activity of human apurinic endonuclease Ape1. J Mol Biol 2003;330(5):1027–1037; doi: 10.1016/S0022-2836(03)00712-5

Yang JL, Chen WY, Mukda S, et al. Oxidative DNA damage is concurrently repaired by base excision repair (BER) and apyrimidinic endonuclease 1 (APE1)-initiated nonhomologous end joining (NHEJ) in cortical neurons. Neuropathol Appl Neurobiol 2020;46(4):375–390; doi: 10.1111/NAN.12584

Yoon JH, De S, Srikantan S, et al. PAR-CLIP analysis uncovers AUF1 impact on target RNA fate and genome integrity. Nat Commun 2014;5:5248; doi: 10.1038/ncomms6248

Address correspondence to:
Prof. Gianluca Tell
Laboratory of Molecular Biology and DNA Repair
Department of Medicine (DAME)
University of Udine
Piazzale M. Kolbe 4
Udine 33100
Italy

E-mail: gianluca.tell@uniud.it

Date of first submission to ARS Central, July 19, 2022; date of acceptance, February 14, 2023.

Abbreviations Used

AP = apurinic and apyrimidinic site
APE1 = apurinic-apyrimidinic endodeoxyribonuclease 1
AUF1 = AU-rich element RNA-binding protein 1
BER = base excision repair
BSA = bovine serum albumin

Abbreviations Used (Cont.)

CGDS = Cancer Genomics Data Server
D:R = DNA:RNA
dNMP = deoxyribonucleosides monophosphate
dNTPs = deoxyribonucleosides triphosphate
DRIP = D:R immunoprecipitation
EDTA = ethylenediaminetetraacetic acid
EMSA = electrophoretic mobility shift analysis
FBS = fetal bovine serum
GBM = glioblastoma
Gdn-HCl = guanidine hydrochloride
GST = glutathione S-transferase
LGG = lower grade glioma
MS/MS = tandem mass spectrometry
MSKCC = Memorial-Sloan-Kettering Cancer Center
NCE = nuclear cell extracts
NIR = nucleotide incision repair
ODN = oligonucleotide
PBS = phosphate-buffered saline
PI = protease inhibitor
PLA = proximity ligation analysis
PMSF = phenylmethylsulfonyl fluoride
Pol β = polymerase β
rAP = ribose monophosphate abasic (both apurinic and apyrimidinic) sites
RER = ribonucleotide excision repair
rNMPs = ribonucleosides monophosphate
rNTPs = ribonucleosides triphosphate
SD = standard deviation
SDS-PAGE = sodium dodecyl sulfate–polyacrylamide gel electrophoresis
siAPE1 = silenced for APE1
siAUF1 = silenced for AUF1
SWB = Southwestern blot
TCGA = The Cancer Genome Atlas
TEAB = triethylammonium bicarbonate
Top1 = topoisomerase 1
UV = ultraviolet
WCE = whole cell extracts